# Oxygen fugacity of global ocean island basalts

**Lori N. Willhite[1]*, Ricardo Arevalo, Jr.[1], Phil Piccoli[1], John C. Lassiter[2], Devin Rand[3], Matthew G. Jackson[3], James M.D. Day[4], Robert W. Nicklas[4], Marek Locmelis[5], Thomas J. Ireland[6], and Igor S. Puchtel[1]**

**Affiliations**
[1]Department of Geology, University of Maryland, College Park, MD 20742
[2]Jackson School of Geosciences, University of Texas, Austin, TX 78712
[3]Department of Earth Science, University of California, Santa Barbara, CA 93117
[4]Scripps Institution of Oceanography, University of California San Diego, La Jolla, CA 92093
[5]Missouri University of Science & Technology, Rolla, MO 65409
[6]Department of Earth and Environment, Boston University, Boston, MA

Corresponding author: Lori Willhite (lnw@umd.edu)

**Key Points:**

- Oxygen fugacity generally does not correlate with radiogenic isotopic compositions that trace recycled material in mantle-derived rocks
- HIMU and EM2 ocean island basalts are more oxidized than EM1 or geochemically depleted ocean island basalts and mid-ocean ridge basalts

## Abstract

Mantle plumes contain heterogenous chemical components and sample variable depths of the mantle, enabling glimpses into the compositional structure of Earth's interior. In this study we evaluate ocean island basalts (OIB) from nine plume locations to provide a global, systematic assessment of the relationship between $fO_2$ and He-Sr-Nd-Pb-W-Os isotopic compositions. Ocean island basalts from the Pacific (Austral Islands, Hawaii, Mangaia, Samoa, Pitcairn), Atlantic (Azores, Canary Islands, St. Helena) and Indian Oceans (La Réunion) reveal that $fO_2$ in OIB is heterogeneous both within and among hotspots. Taken together with previous studies, global OIB have elevated and heterogenous $fO_2$ (average = +0.5 ΔFMQ; 2SD = 1.5) relative to prior estimates of global mid-ocean ridge basalts (MORB; average = -0.1 ΔFMQ; 2SD = 0.6), though many individual OIB overlap MORB. Specific mantle components, such as HIMU and EM2 that are defined by radiogenic Pb and Sr isotopic compositions compared to other OIB, respectively, have distinctly high $fO_2$ based on statistical analysis. Elevated $fO_2$ in OIB that sample these components is associated with higher whole-rock $CaO/Al_2O_3$ and olivine CaO content, which may be linked to recycled carbonated oceanic crust. EM1-type and geochemically depleted OIB are generally not as oxidized, possibly due to limited oxidizing potential of the recycled material in the EM1 component (e.g., sediment) or lack of recycled materials in geochemically depleted OIB. Despite systematic offset of the $fO_2$ among EM1-, EM2-, HIMU-type OIB, geochemical indices of lithospheric recycling, such as Sr-Nd-Pb-Os isotopic systems, generally do not correlate with $fO_2$.


## Plain Language Summary

Rocks from Earth's surface are mixed back into the interior during crustal recycling. For example, plate tectonics results in subduction of oceanic crust back into the mantle. Recycling of surface materials might oxidize the interior of the Earth. Mantle plumes, which are buoyantly rising portions of the mantle that create ocean islands like Hawaii, Iceland, Samoa, etc., contain the chemical and isotopic characteristics associated with recycled materials in their sources. Here we investigate rocks from mantle plumes that have heterogeneous isotopic compositions as a result of incorporating different types of recycled lithosphere to test whether their oxygen fugacity varies systematically with the type of recycled crust in their source. We show that some types of mantle plume-derived rocks, called HIMU and EM2 characterized by their extreme isotopic compositions,

are more oxidized than the EM1 or typical, geochemically depleted rocks from mantle plumes and from spreading centers in the oceans. These results link recycled materials to oxidation of Earth's mantle.

## 1 Introduction

In planetary systems, oxygen fugacity ($fO_2$) is a chemical parameter that affects the speciation, geochemical behavior, and physical distribution of multivalent trace elements among key chemical reservoirs, such as Earth's metallic core, rocky mantle and crust, liquid water ocean, and gaseous atmosphere. For example, mantle $fO_2$ influenced the speciation of volcanic gases that made up Earth's early atmosphere (French, 1966; Kump et al., 2001; Hirschmann, 2012). Mantle $fO_2$ and dynamics may be linked to the oxygenation of the atmosphere (Kasting et al., 1993; Andrault et al., 2018; Kadoya et al., 2020; Ortenzi et al., 2020; O'Neill and Aulbach, 2022). Plate tectonics has been invoked to explain why Earth is more oxidized and has more $fO_2$ variability compared to Mars (Righter and Drake, 1996). Rocks from Earth's surface are mixed back into the mantle, potentially modifying and regulating the $fO_2$ of the interior (e.g., Kasting et al., 1993; Lécuyer and Ricard, 1999; Evans, 2012). If recycliong of lithosphere is responsible for regulating and/or modifying mantle $fO_2$, there may be a link between plate tectonics, mantle $fO_2$, and planetary habitability (Cockell et al., 2016).

The presence of recycled lithosphere in plume components has been identified using radiogenic isotopic compositions like $^{87}Sr/^{88}Sr$, $^{143}Nd/^{144}Nd$, $^{187}Os/^{188}Os$, and $^{206,207,208}Pb/^{204}Pb$. These isotopic ratios have been used to define mantle components, including enriched mantle 1 (EM1), enriched mantle 2 (EM2), high-μ (HIMU; where $\mu = {}^{238}U/^{204}Pb$), which may result from recycling of different types of lithosphere (Zindler and Hart, 1986; Hart et al., 1992; Hofmann, 1997). By contrast, relatively well preserved mantle domains (i.e., that have not been modified by mixing with significant mass of recycled materials) host primitive isotopic signatures, such as high $^{3}He/^{4}He$ and anomalous $\mu^{182}W$ (Kurz et al., 1982; Zindler and Hart, 1986; Hart et al., 1992; Farley et al., 1992; Mundl et al., 2017; Jackson et al., 2020). Recycled lithosphere in mantle plume sources might have played a role in generating higher $fO_2$ observed at Hawaii, Iceland, Canary, and Cape Verde relative to MORB (Moussallam et al., 2014, 2016, 2019; Shorttle et al., 2015; Helz et al., 2017; Brounce et al., 2017; Hartley et al., 2017; Taracsák et al., 2022; Nicklas et al., 2022b). However, not all individual OIB lavas are oxidized relative to MORB, which may reflect a lesser

proportion of oxidized material and/or different types of recycled material in their respective source regions; and/or, derivation via petrogenetic processes that lower $fO_2$, such crustal assimilation (Brounce et al., 2022; Nicklas et al., 2022a). Chemical fingerprints of crustal and mantle materials in OIB, particularly He-Sr-Nd-W-Os-Pb isotopic compositions, allow for exploration of prospective links between mantle $fO_2$ and lithosphere recycling.

To probe the roles of distinct Earth materials in the evolution of $fO_2$ in the planet's interior, this study systematically explores the $fO_2$ of a diverse, global suite of plume-derived lavas from the Canary, Samoa, La Réunion, Hawaii, Azores, Pitcairn, St. Helena, and Macdonald hotspots (**Figure 1**). Mangaia and the Austral Islands of Rapa Iti and Raivavae, which are all products of the Macdonald hotspot, are considered individually because the lavas from Mangaia have distinctly high $fO_2$ (and loss on ignition, indicating high degrees of alteration and warranting cautious interpretation). Despite forming part of a continental flood basalt province, lavas from Baffin Island are also included in this survey because they sample the proto-Iceland plume and offer useful insights relative to OIB due to their high-$^3He/^4He$—a signature of ancient mantle preservation (Starkey et al., 2009; Willhite et al., 2019).

This study leverages the olivine-melt partition coefficient of redox-sensitive V ($D_V^{ol/melt}$) to characterize the $fO_2$ of global mantle components, including depleted mantle, EM1, EM2, and HIMU. Vanadium primarily exists as a +3 or +4 cation in terrestrial magma systems (Borisov et al., 1987; Gaetani and Grove, 1997). Under oxidizing conditions, a higher proportion of V exists at the higher valence state, resulting in a net change in the size-to-charge ratio that renders V largely incompatible in olivine during melt crystallization (Canil, 1997). By contrast, under reducing conditions $V^{3+}$ can substitute more readily for $Mg^{2+}$ and $Fe^{2+}$ in the olivine lattice. Experimental studies have shown that V partitioning between olivine and melt is relatively insensitive to bulk composition, pressure, and temperature during basalt petrogenesis (Canil, 1999; Canil and Fedortchouk, 2001; Righter et al., 2006b, 2006a; Suzuki and Akaogi, 1995; Wang et al. 2019). Olivine is an early crystallizing phase in magmatic systems and V is relatively immobile during metamorphism (Condie, 1976). Due to these characteristics, $fO_2$ signatures recorded by the most primitive (i.e., most Mg-rich and earliest crystallizing) olivine are representative of the original magma and resistant to post-magmatic processes, such as low-to-moderate degrees of

111 oxide accumulation (<5 modal %), sulfur saturation, degassing, or metasomatism (Locmelis et al.,
112 2019).

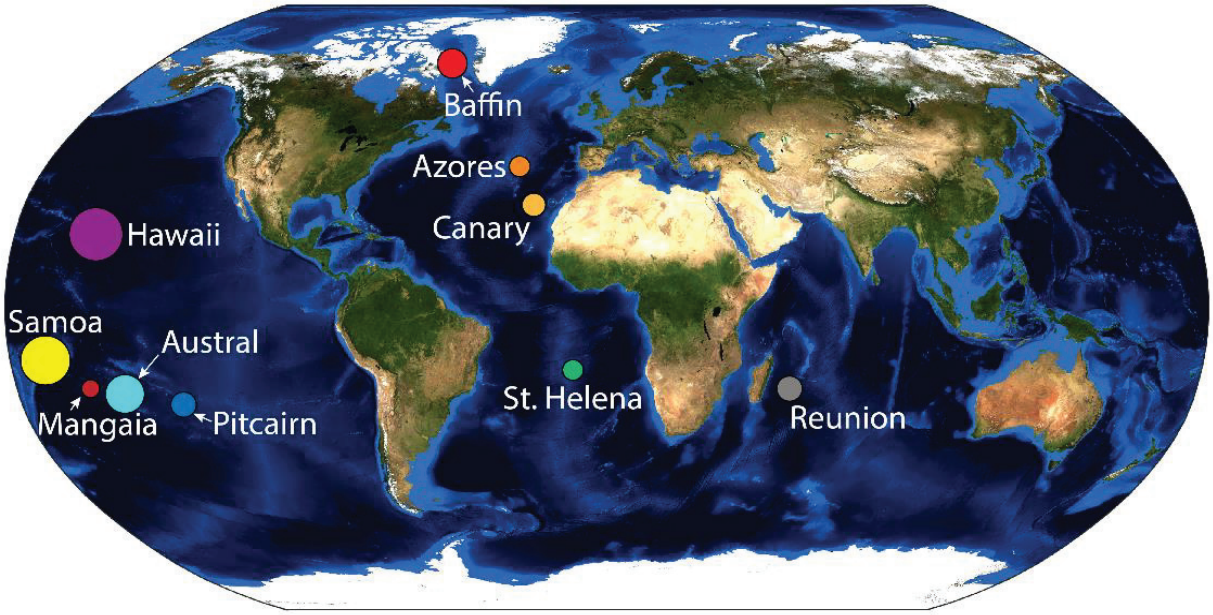


113

114 **Fig 1. Map of global OIB localities with new $fO_2$ data presented in this study**. The size of the circle at each site
115 corresponds to the number of analyses from that hotspot. Earth image is from the NASA Earth Observatory *Blue*
116 *Marble* series.

117 ## 2 Materials and methods

118 ### *2.1. OIB in this study*

119 The 56 rocks studied here compose a global sample suite of OIB from nine mantle-plume-
120 associated hotspots: Azores, Canary, Hawaii, Iceland (proto-Iceland plume lavas from Baffin
121 Island), Macdonald (including Mangaia and the Austral Islands of Raivavae and Rapa Iti), Pitcairn,
122 La Réunion, Samoa, and St. Helena. Samples were selected based on the availability of previously
123 published major, minor, and trace element data, as well as isotopic compositions (**see**
124 **Supplementary Tables S1 and S2, respectively**). Primitive samples with limited evidence of
125 pyroxene fractionation were targeted. Forty-two samples have whole-rock MgO contents greater
126 than 9.0 wt. %; seven samples from Baffin Island are vitrophyres with MgO wt. % between 7.9
127 and 9.4; and three samples (KOO-01; PIT-3, CE-13) are slightly more evolved (5.2 to 7.7 wt. %

MgO). Four lavas do not have published whole-rock MgO wt. %. Both subaerial and submarine lavas are included (**Table 1**). Photomicrographs and scans of epoxy-mounted rock fragments are provided for a subset of the lavas (**Supplementary Figures S1-S2**).

**Table 1.** New oxygen fugacity data and most primitive olivine Fo# measured in each OIB.

| Location | Sample | Eruption environment | Mantle component | [1]Olivine Fo# | ΔNNO | ΔFMQ | 2SD[2] |
|---|---|---|---|---|---|---|---|
| Austral | RPA488 | subaerial | EM1 | 83 | 0.6 | 1.3 | 0.2 |
| Austral | RPA502 | subaerial | EM1 | 84 | 0.5 | 1.2 | 0.3 |
| Austral | RPA367 | subaerial | EM1 | 83 | -0.1 | 0.6 | 0.3 |
| Austral | RVV318 | subaerial | HIMU | 84 | -0.1 | 0.6 | 0.5 |
| Austral | RVV321 | subaerial | HIMU | 84 | 0.0 | 0.7 | 0.2 |
| Austral | RV310 | subaerial | | 83 | 0.5 | 1.3 | 0.4 |
| Austral | RV346 | subaerial | HIMU | 82 | 0.8 | 1.5 | 0.8 |
| Azores | TR0802 | subaerial | | 91 | 1.0 | 1.7 | 0.3 |
| Azores | PX0802 | subaerial | | 84 | 0.3 | 1.1 | 0.7 |
| Azores | PX0801 | subaerial | | 84 | 0.6 | 1.4 | 0.3 |
| Baffin | PD13 | submarine | | 89 | -0.1 | 0.6 | 0.7 |
| Baffin | PD-14 | submarine | | 85 | 0.0 | 0.8 | 0.3 |
| Baffin | PD-19 | submarine | | 89 | -0.1 | 0.6 | 0.4 |
| Baffin | PD-21 | submarine | | 87 | 0.1 | 0.8 | 0.4 |
| Baffin | PD-24 | submarine | | 89 | 0.5 | 1.2 | 0.5 |
| Baffin | PD-29 | submarine | | 88 | 0.5 | 1.2 | 0.2 |
| Baffin | PD-64 | submarine | | 85 | 0.0 | 0.8 | 0.9 |
| Canary | LP-01 | subaerial | | 82 | 0.7 | 1.4 | 0.3 |
| Canary | LP-09 | subaerial | HIMU | 86 | 1.6 | 2.4 | 1.0 |
| Canary | EH-07 | subaerial | | 79 | 1.4 | 2.2 | 0.7 |
| Canary | EH-10 | subaerial | | 76 | 0.6 | 1.3 | 0.5 |
| Hawaii | H-2 | submarine | | 90 | 0.5 | 1.2 | 0.3 |
| Hawaii | H-7 | submarine | | 89 | 0.6 | 1.4 | 0.6 |
| Hawaii | H-9 | submarine | | 88 | 0.4 | 1.1 | 0.8 |
| Hawaii | H-11 | submarine | | 88 | 0.6 | 1.3 | 0.4 |
| Hawaii | H-27 | submarine | | 87 | 0.1 | 0.8 | 0.9 |
| Hawaii | H-P | submarine | | 87 | 0.2 | 0.9 | 0.1 |
| Hawaii | Kil-1-18 | submarine | | 90 | 0.9 | 1.7 | 0.3 |
| Hawaii | Kil-2-3 | submarine | | 89 | 0.6 | 1.3 | 0.7 |
| Hawaii | Kil-2-4 | submarine | | 88 | 0.9 | 1.6 | 0.7 |
| Hawaii | Kil-3-1 | submarine | | 88 | 0.8 | 1.5 | 0.2 |
| Hawaii | Kil-1840-2 | subaerial | | 87 | 0.3 | 1.0 | 0.7 |
| Hawaii | KOO-01 | subaerial | | 83 | -0.3 | 0.4 | 0.9 |
| Hawaii | KOO-17A | subaerial | | 89 | -0.1 | 0.7 | 0.5 |
| Hawaii | K500-5B | submarine | | 90 | 0.5 | 1.2 | 0.5 |

| | | | | | | | |
|---|---|---|---|---|---|---|---|
| Hawaii | K497-6 | submarine | | 87 | -0.1 | 0.6 | 0.4 |
| Mangaia | MG1002 | subaerial | HIMU | 81 | 1.5 | 2.2 | 0.2 |
| Mangaia | MG1001 | subaerial | HIMU | 81 | 1.7 | 2.4 | 0.2 |
| Pitcairn | PIT-11 | subaerial | EM1 | 80 | 0.3 | 1.1 | 0.3 |
| Pitcairn | PIT-8 | subaerial | EM1 | 80 | -0.1 | 0.6 | 0.5 |
| Pitcairn | PIT-3 | subaerial | EM1 | 79 | 0.2 | 0.9 | 0.3 |
| Reunion | RU0714 | subaerial | | 88 | 0.6 | 1.3 | 0.1 |
| Reunion | RU0710 | subaerial | | 88 | 1.3 | 2.0 | 0.5 |
| Reunion | RU0702 | subaerial | | 83 | 0.5 | 1.2 | 0.4 |
| Samoa | T16 | subaerial | EM2 | 85 | 0.7 | 1.5 | 0.2 |
| Samoa | T25 | subaerial | EM2 | 84 | 1.2 | 1.9 | 0.3 |
| Samoa | T33 | subaerial | EM2 | 86 | 0.9 | 1.6 | 0.5 |
| Samoa | AVON3-78-1 | submarine | EM2 | 83 | 0.9 | 1.6 | 0.5 |
| Samoa | AVON3-76-9 | submarine | EM2 | 84 | 0.7 | 1.5 | 0.9 |
| Samoa | AVON3-68-11 | submarine | EM2 | 90 | 0.4 | 1.1 | 0.3 |
| Samoa | AVON3-63-11 | submarine | EM2 | 90 | 1.5 | 2.2 | 0.4 |
| Samoa | OFU-04-03 | subaerial | EM2 | 84 | 0.9 | 1.6 | 0.1 |
| St. Helena | CE-3 | | HIMU | 84 | -0.2 | 0.5 | 0.3 |
| St. Helena | CE-9 | subaerial | HIMU | 83 | -0.1 | 0.7 | 0.2 |
| St. Helena | CE-10 | | HIMU | 82 | -0.2 | 0.6 | 0.4 |
| St. Helena | CE-13 | subaerial | HIMU | 74 | 0.18 | 0.90 | 0.03 |

The $fO_2$ shown here is calculated using the partition coefficient of V between modelled parental melt and V measured in the most primitive (highest Fo#) olivine from each sample, which includes all grains whose Fo# is within analytical uncertainty of the highest Fo# olivine. Data for all olivines and other trace elements analyzed in this study can be found in the supplementary material.

[1]Samples that do not have a mantle component listed are considered geochemically depleted (see Section 2.7.).

[1]Fe and Mg were measured via electron probe microanalysis; olivine V concentrations were measured via laser-ablation medium-resolution inductively coupled plasma mass spectrometry (see methods).

[2]Uncertainties represent either the external reproducibility of $fO_2$ calculated among primitive olivine from a single sample or the average prediction uncertainty of each calculated $fO_2$ (see Section 2.6.), whichever is greater. Samples with a single olivine analysis have only the prediction uncertainty from the calculated $fO_2$.

### *2.2. Olivine and basaltic matrix major element analyses*

Basaltic samples were cut, mounted in one-inch diameter epoxy mounts, and abraded with alumina powder (down to 1 um particle size) so that visible olivine crystals were exposed and polished. The polished samples were cleaned via Milli-Q water (18.2 MΩ·cm) in an ultrasonic bath, and carbon coated for electron probe microanalysis (EPMA) using the *JEOL 8900R* electron microprobe in the *Advanced Imaging and Microscopy Laboratory* at the University of Maryland, USA. All analyses were performed using a 15 kV potential and 20 nA current measured at the

faraday cup. Matrix and olivine analyses were acquired using a 10 and 2 micron diameter beam, respectively.

To determine the major element composition of basaltic matrices, the crystalline groundmass of each sample was analyzed using four lines comprising ten equally spaced analytical spots. Analytical uncertaines were typically less than 2%. Phenocrystic olivine was avoided during measurement of the matrix composition in order to determine how V paritions between olivine and the melt. Primary standards for the matrix analyses included Makapuhi Lava Lake basalt glass (USNM: VG-99), Indian Ocean basalt glass (USNM: 113716) and Broken Hill rhodonite (USGS PXBX).

Depending on the size of the phenocryst, each olivine grain was analyzed in one to three sites located away from features such as microfractures, reaction rims, and/or inclusions when observed; each site was characterized by four independent spot measurements. When only a single site was analyzed, the olivine core was sampled. For grains that were large enough, the core and rim were targeted to investigate chemical gradients in zoned olivine, though few samples exhibited appreciable differences in V concentrations between the core and rim. Primary standards for the olivine analyses included San Carlos (USNM 111312/444) and Rockport (USNM 85276) olivines, and Kakanui hornblende (USNM 122142).

### *2.3. Olivine and basaltic matrix trace element analyses*

First-row transition elements (FRTE; Sc, Ti, V, Cr, Mn, Fe, Co, Ni, Cu, Zn) and Ga and Ge were measured in olivine grains ($n$ = 257 grains) and sample matrix (i.e., crystalline groundmass) by laser ablation (LA-) and medium-resolution inductively coupled plasma mass spectrometry (ICPMS) using either the *New Wave UP213* laser system coupled to the *Thermo Fisher Scientific Element 2* mass spectrometer housed in the *Plasma Lab* at the University of Maryland, or the *Photon Machines Analyte G2* laser system coupled to the *Nu AttoM* mass spectrometer housed in the *Planetary Environments Lab* at NASA Goddard Space Flight Center, Maryland, USA. Each sample was characterized following the analytical protocol of Arevalo et al. (2011), whereby multiple reference materials (i.e., USGS basaltic reference glasses BHVO-2G, BIR-1G and BCR-2G) were used to build a sensitivity calibration curve, rather than relying on only a single bracketing standard to quantify elemental abundances. The measured isotopes for each element were $^{45}$Sc, $^{47,49}$Ti, $^{51}$V, $^{52,53}$Cr, $^{55}$Mn, $^{56,57}$Fe, $^{59}$Co, $^{60,62}$Ni, $^{63,65}$Cu, $^{66,67,68}$Zn, $^{69,71}$Ga,

$^{72,73,74}$Ge, $^{75}$As, $^{77}$Se, and $^{43}$Ca as the internal standard. Laser parameters used were: 2 – 3 J/cm$^2$ fluence; 10 Hz repetition rate; and a spot size between 150 – 250 microns in diameter to maximize count rates. The plasma source of the mass spectrometer was tuned to maximize ionization, as monitored by $^{43}$Ca and $^{232}$Th count rates, while maintaining limited oxide production ($^{232}$Th$^{16}$O/$^{232}$Th ≤ 0.20%). New olivine and matrix data are provided in **Supplementary Table S3 and S4**, respectively.

### *2.4. Petrologic modelling to determine olivine V partition coefficients*

The measured V, MgO, and FeO abundances in each matrix and olivine pair are used as starting points to model the parental melt of each respective olivine. The aim of the model is to determine the V concentration and Mg# of each olivine's parental melt and determine $D_V^{ol/melt}$. To model the melt composition that is in equilibrium with each individual olivine, olivine is iteratively added or subtracted from the measured matrix composition. Each iteration adds 0.1% of the equilibrium olivine composition to the matrix. The FeO and MgO composition of the equilibrium olivine is calculated based on an Fe-Mg partitioning coefficient of 0.31 (Roeder and Emslie, 1970). Here, the total FeO of the matrix is used to calculate the Fe-Mg partition coefficient because the $Fe^{2+}/Fe^{3+}$ of the matrix is unknown. This can result in a higher calculated $fO_2$; thus, the final calculated $fO_2$ may reflect a maximum estimate for the parental melt. Paired $Fe^{2+}/Fe^{3+}$ and $D_V^{ol-melt}$ may be an improvement for future studies. The $SiO_2$ of equilibrium olivine in each step is calculated by substracting the FeO and MgO wt. % from 100. . The V concentration of the equilibrium olivine at each melt stage is based on empirical relationships observed between olivine forsterite content and V concentration for each locality (**Figure 2**). As the equilibrium olivine composition changes throughout the model, the empirical regressions are used to determine the corresponding olivine V concentration. Regression parameters used to calculate V concentration as a function of olivine Fo# (Fo# = molar Mg/(Mg + Fe)) for each locality are recorded in **Supplementary Table S5**. The model is further described in the schematic in **Supplementary Figure 3** and resulting parental melt V concentration and final olivine V concentration are reported **in Supplementary Table S6**.

Other major elements (e.g., $TiO_2$, $Al_2O_3$, MnO, CaO, $Na_2O$, $K_2O$, and $P_2O_5$), do not affect the modelled olivine composition or the calculated V partition coefficient; therefore, the matrix was not characterized by EPMA in this study. In order to provide a parental melt composition for

all major elements, the published whole-rock data are used. Throughout the petrolgic model, olivine dilutes the $TiO_2$, $Al_2O_3$, MnO, CaO, $Na_2O$, $K_2O$, and $P_2O_5$ as the olivine FeO, MgO, and $SiO_2$ is added to the matrix. In each iteration of the model, the $TiO_2$, $Al_2O_3$, MnO, CaO, $Na_2O$, $K_2O$, and $P_2O_5$ content are reduced by 0.1% as 0.1% olivine is added. The full parental melt compositions are reported in **Supplementary Table S6.**

### *2.5. Oxygen fugacity calculation*

The relationship between oxygen fugacity and $D_V^{ol/melt}$ has been empirically derived (Canil, 1997; Canil and Fedortchouk, 2001; Mallmann and O'Neill, 2009, 2013; Wang et al., 2019). Experimental data are limited in the higher $fO_2$ range that is observed in OIB leading to higher uncertainties in the higher $fO_2$ range. This affects the calculations reported here (details provided below). Experimental calibrations at higher $fO_2$ would increase the fidelity and reduce the uncertainty of quantitative $fO_2$ derivations in future work. This study uses the regression equation (**Equation 1**) from Nicklas et al. (2019) that includes data from previous experimental studies compiled in Nicklas et al. (2018). In this equation, $fO_2$ is calculated relative to the nickel-nickel oxide buffer (ΔNNO).

$$\mathrm{Log}\, D_V^{ol-melt} = -2.50 \pm 0.23 \times \Delta NNO - 1.501 \pm 0.064 \quad (r^2 = 0.94) \qquad \textbf{(Eq. 1)}$$

The final reported $fO_2$ for each sample is the average determined by the most primitive (highest Fo#) olivine(s) from that rock (**Table 1**). Using only the most primitive olivines as representative of the earliest solids derived from the parental melt limits potential effects of clinopyroxene and oxide fractionation on the olivine V concentration. Out of caution, olivine with anomalous Ti, Cu, or Cr contents (defined outside 3 × the interquartile range) are not used to calculate oxygen fugacity to avoid the possibility that an oxide or sulfide inclusion was sampled by the laser during LA-ICPMS. A total of 200 primitive olivines are used to calculate the $fO_2$ of the 56 lavas in this study (**Supplementary Table S7**). In arc lavas, V partitioning is dependent on temperature (*T*) and melt polymerization (quantified as the ratio of non-bridging oxygen to total tetrahedrally coordinated cations, *NBO/Tot*) in addition to oxygen fugacity (Wang et al., 2019), per the expression:

$$\Delta\mathrm{FMQ} = \left(\mathrm{Log}\, D_V^{ol-melt} + 2.3 - \left(\frac{1871}{T(K)}\right) + 0.24 \times \left(\frac{NBO}{Tot}\right)\right)/-0.258 \qquad \textbf{(Eq. 2)}$$

**Equation 2** is used to calculate $fO_2$ relative to the fayalite-magnetite-quartz buffer. For the subset of lavas in this study that have complete major element datasets ($n$ = 50), we applied both **Equation 1 and 2** to check for consistency (**Supplementary Table S8**). All but one lava (Samoan sample AVON3-68-11) have overlapping $fO_2$ within uncertainty using the two empirical relationships (**Supplementary Figure S4**). Sample AVON3-68-11 has the highest NBO/Tot and melting temperature calculated using Petrolog3 software (Danyushevsky and Plechov, 2011). Given that both equations give consistent $fO_2$ for almost all lavas, this study uses **Equation 1** to include the lavas that do not have complete major element data.

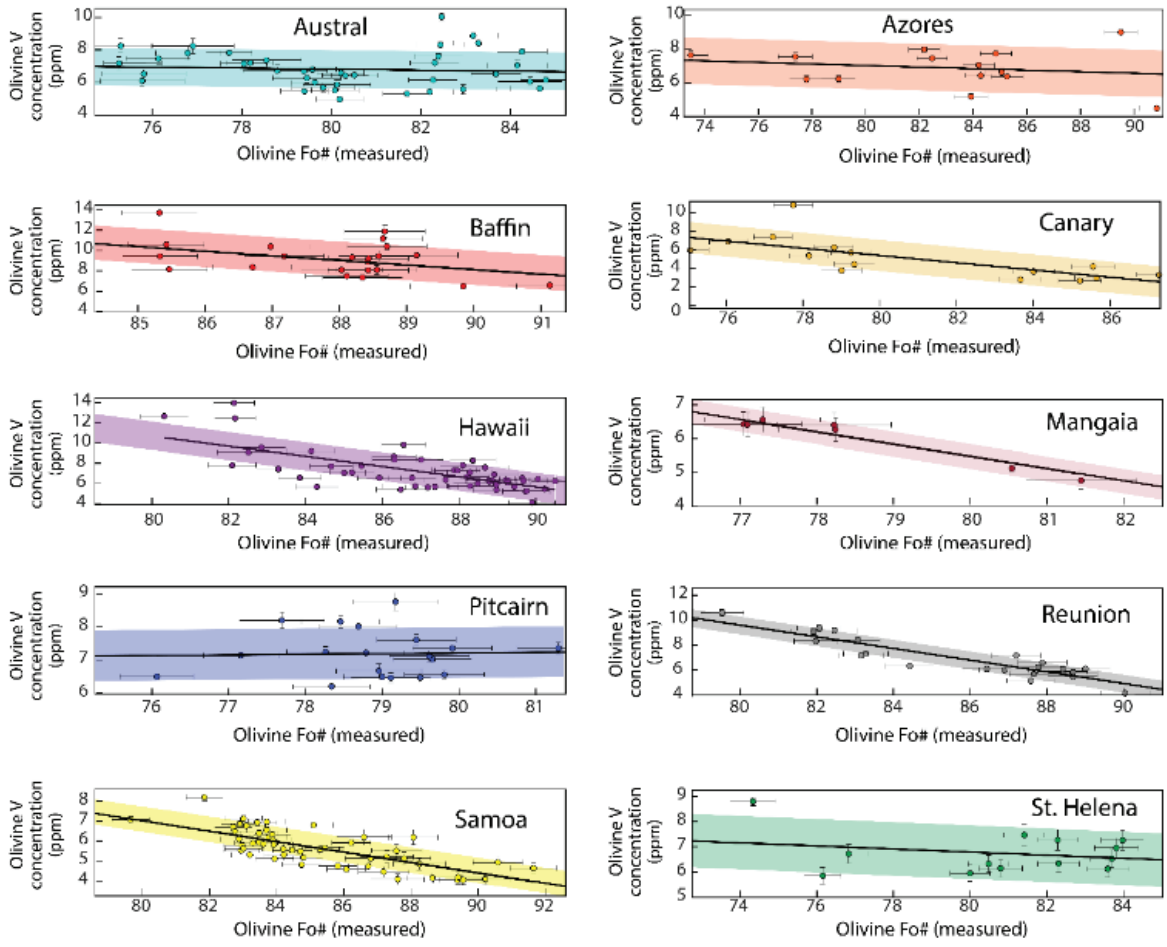


**Fig 2. Linear regressions for each locality used to carry out petrologic models** (see methods for details). The shaded fields represent the prediction uncertainty (RMSE) obtained using the Jack-knifing technique described in section 2.6. The prediction uncertainty is the error associated with using a Fo# to predict a V concentration to model the parental melt. This uncertainty is propagated through the melt model and calculation of $fO_2$. Regression parameters for each locality are given in **Supplementary Table S1**.

### *2.6. Evaluation of Uncertainty*

In order to investigate the statistical robustness of possible distinctions in $fO_2$ between different OIB localities (as well as individual samples from the same locality), a comprehensive analysis of uncertainties and error propagation is essential. To constrain the uncertainty associated with the linear regression for olivine V ppmw versus Fo# (Step 1 in the petrologic modelling; **Supplementary Figure 3**), we employ cross validation (or jack-knifing) and Monte Carlo sampling of the analytical errors associated with each olivine and matrix measurement. To include the analytical errors associated with measurment of olivine V concentration and Fo#, we employ Monte Carlo sampling of of the V and Fo# uncertainties during each iteration of the Jack-knifing routine. In each iteration of the Jack-knifing routine, each datum can fall anywhere within the 95% confidence interval of its analytical uncertainty. Jack-knifing iteratively leaves out one data point at a time and the number of iterations is equal to the total number of data.

The final regression parameters for each locality are the means of the sampled parameters, and the final error is the root mean square error (RMSE) of the regression line relative to the validation point (i.e., the datum that is left out in any given iteration). The RMSE is propagated through the petrologic model provided here to constrain the uncertainty on the modelled V partition coefficient between olivine and parental melt, which is then propagated through **Equation 1**. The parameter uncertainties for **Equation 1** reported in Nicklas et al. (2018) are incorporated into the final calculation. The final uncertainty for each rock is either the external reproducibility (i.e., the standard deviation of the $fO_2$ from different olivines within the rock) or the prediction uncertainty from the $fO_2$ calculation (described here), whichever is greater. The $fO_2$ and uncertainty for each rock is reported in **Table 1**.

Olivine from St. Helena, Azores, Pitcairn, and Austral have regressions with high p values (**Figure 2**), which indicate olivine Fo# and olivine V concentration are not well correlated. This likely indicates that the individual samples defining each curve are not cogenetic. However, the data can still be used to model the parental melt because the petrologic model only needs to predict the V concentration of the equilibrium olivine in each step within the 95% confidence interval. Thus, the model still determines the V concentration of the equilibrium olivine for the parental melt within the confidence interval. High p values and scatter in the data will lead to higher uncertainties associated with the linear regression, which are propagated through the model.

### *2.7. Grouping lavas into mantle components*

To simplify the investigation of the effect of recycled materials on $fO_2$, we examine individual mantle components by grouping lavas from this study and our compilation of previous studies into HIMU, EM1, EM2, or geochemically depleted OIB to identify if these components have distinct $fO_2$. Lavas are considered HIMU if their $^{206}Pb/^{204}Pb$ is >20 (e.g., Jackson et al., 2018). EM1 lavas are identified by moderately to highly radiogenic $^{87}Sr/^{86}Sr$ and unradiogenic $^{143}Nd/^{144}Nd$ with a Sr-Nd slope of ~-0.28; EM2 lavas are categorized by extreme $^{87}Sr/^{86}Sr$ and moderate $^{143}Nd/^{144}Nd$ with a Sr-Nd slope of ~-0.06 (Zindler and Hart, 1986). **Supplementary Figure 5** illustrates the distinct trajectories that define EM1 and EM2 lavas in this study. Lavas that have $^{87}Sr/^{86}Sr$ <0.7044, $^{143}Nd/^{144}Nd$ >0.5128, and $^{206}Pb/^{204}Pb$ is <20 are grouped together as geochemically depleted lavas. The geochemically depleted group may include lavas that have isotopic compositions described as "FOZO" (focus zone), which is the isotopic composition where OIB Sr-Nd-Pb arrays appear to converge (Hart et al., 1992). Lavas that have "FOZO" compositions are grouped with geochemically depleted lavas here because they do not contain definitive evidence of recycled material in their sources based on canonical isotopic signatures. This is not meant to imply that all grouped lavas are derived from a uniform or shared physical reservoir. For the purpose of discerning $fO_2$ among types of recycled material, we assume individual lavas belong to only one mantle component (i.e., samples are not mixtures of multiple components). The component type assigned to each lava in this study is given in **Table 1** and illustrated in **Supplementary Figure 5**.

### *2.8. Statistical tests*

To test the statistical independence of different localities and mantle components with respect to inferred source $fO_2$, quantified relative to the fayalite-magnetite-quartz buffer (ΔFMQ), we used a one-way analysis of variance (ANOVA) test. The one-way ANOVA test compares mean values to test whether data in categorical groups (in this case, OIB localities) have the same mean (the null hypothesis), or if at least one group has a distinct mean. To test the significance of correlations between $fO_2$ and isotope systems (He-Sr-Nd-W-Os-Pb), we use the square of Pearson's correlation coefficients ($r^2$) and the associated p value. P-values quantify the probability that the regression can predict the dependent variable (i.e., an isotopic composition) by incorporating the independent variable (i.e., $fO_2$) better than by relying on a degenerate model

(e.g., the average value of the dependent variable). In this case, p values greater than 0.05 indicate that the regression is not statistically significant at the 95% confidence interval, while p values less than 0.05 indicate that the correlation is significant at the 95% confidence interval. In this study, a significant p value means that $fO_2$ can predict a given isotopic, trace element, or major element composition better than relying on the average composition. Because Pearson's correlation coefficients assume a linear relationship, we also investigated non-parametric correlation tests, such as Spearman's correlation coefficient and Kendall's Tau; the findings remain the same.

## 3 Results

### *3.1. New OIB olivine analyses*

New olivine FRTE and Ga, Ge compositions are reported in **Supplementary Table S3** and visualized in **Figure 3**. Forsterite number varies from 74 to 92. Olivines with the lowest and most variable Fo# are from HIMU-type lavas (81.4 ± 7.4 2SD). Geochemically depleted OIB have the highest average Fo# olivine (86.4 ± 7.2 2SD). Vanadium concentrations range from 2.7 to 13.7 ppmw in the global dataset. Mean olivine V concentrations are statistically lower in HIMU and EM2 lavas according to the one-way ANOVA test. Olivines from EM1 and geochemically depleted lavas have similar mean olivine V concentrations. HIMU- and EM2-type lavas are also distinguished from EM1 and geochemically depleted OIB based on olivine CaO that is resolvedly higher in HIMU and EM2 OIB (**Figure 4**). Olivine Ni concentrations are highest and most variable in geochemically depleted OIB, with concentrations ranging from 1100 to 4800 ppmw Ni (0.14 to 0.61 wt. % NiO). The highest Ni contents in olivine in the global dataset are from Hawaii and Baffin Island. Lavas that are HIMU- and EM1-type have olivine with the lowest Ni concentrations on average.

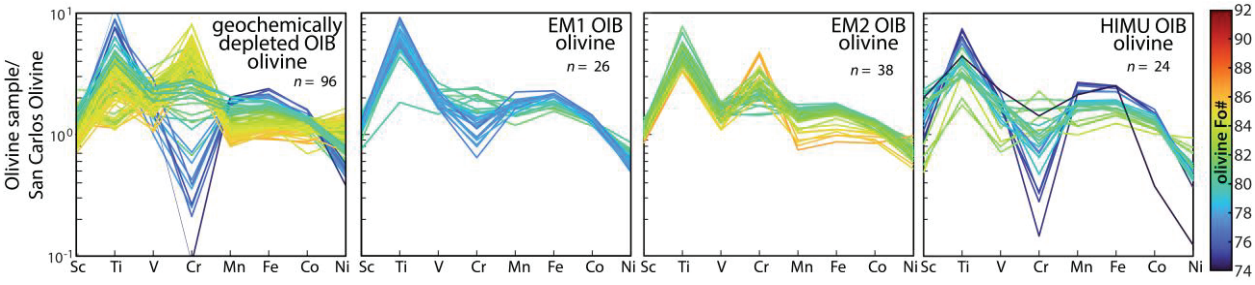


**Fig 3. Olivine first-row transition element compositions normalized to the San Carlos olivine reference material**. Olivines are grouped according to the mantle components of their host lava.

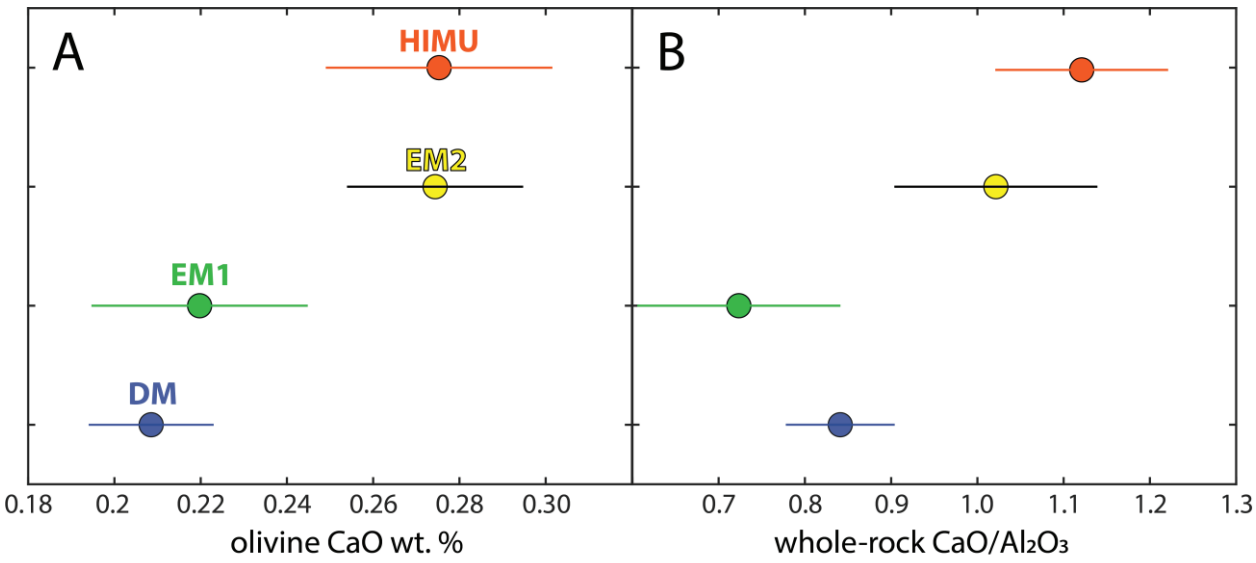


**Fig 4. HIMU and EM2 lavas have high olivine CaO and HIMU has high whole-rock $CaO/Al_2O_3$. (A)** ANOVA results showing the mean (circles) and 95% confidence interval (lines) for the olivine CaO wt. % of each mantle component. If confidence intervals do not overlap, then the respective components have statistically distinct means. **(B)** ANOVA results for whole-rock $CaO/Al_2O_3$ illustrating statistically higher $CaO/Al_2O_3$ in HIMU lavas compared to geochemically depleted OIB and EM1.

### *3.2. Oxygen fugacity of global OIB*

The average $fO_2$ of global OIB in this study is +1.2 ± 0.5 (2SD) ΔFMQ, in agreement with the EM-type and HIMU-type OIB average of +1.5 ± 0.8 ΔFMQ determined by Nicklas et al. (2022). Though $fO_2$ uncertainties and heterogeneity within and among OIB groups is large, making it difficult to draw definitive conclusions, statistical tests indicate that some OIB localities and mantle components have distinct $fO_2$. A summary of which plume locations are statistically distinct is illustrated in **Supplementary Figure S6**. When the new data presented here are combined with a compiled OIB dataset (**Supplementary Table S9**), the mean $fO_2$ of OIB is +0.6 ± 1.1 ΔFMQ. Lavas designated as HIMU have the highest average $fO_2$ of +1.5 ΔFMQ (± 3.0 2SD) and are distinctly oxidized compared to all other mantle components using a one-way ANOVA test (**Figure 5**). EM2 lavas have the second highest $fO_2$ (+0.7 ± 0.7 ΔFMQ) and are oxidized relative to geochemically depleted lavas (-0.3 ± 1.1 ΔFMQ) but are not distinct from EM1 (+0.2 ± 0.6

358 ΔFMQ). The $fO_2$ of OIB is elevated relative to the range for MORB mantle (+0.3 to +0.9 ΔFMQ)
359 estimated using the same proxy and methodology (Nicklas et al., 2019), as well as the global
360 MORB average (-0.1 ± 0.3 ΔFMQ) using a variety of other $fO_2$ proxies (**Figure 5; Supplementary**
361 **Table 10**). The variance of $fO_2$ among all OIB is greater than the variance among MORB samples,
362 possibly related to OIB source heterogeneity and/or complex petrogenesis.

363 Using an independent samples t-test, there is no apparent difference between the $fO_2$
364 inferred from submarine ($n$ = 23) versus subaerial ($n$ = 31) OIB in the dataset presented here. Lavas
365 from Mangaia have notably high LOI—i.e., 6.8 wt.% and 8.8 wt.%—reflecting subaerial alteration
366 (**Supplementary Figure S7**). Though V is robust to subaerial alteration, the calculated $fO_2$ of the
367 Mangaia samples in this study could be affected if $SiO_2$, $FeO_T$, or MgO were decreased or
368 increased by alteration, as this would affect the calculated parental melt composition to determine
369 the V partition coefficient. The $fO_2$ of the Mangaia samples is within error when calculated using
370 Equation 1 and Equation 2. Given that Equation 2 requires the ratio of non-bridging oxygen to
371 total tetrahedrally coordinated cations, the consistency of the calculated $fO_2$ for Mangaia gives
372 confidence that the major element composition, and therefore, $fO_2$, has not been severely affected
373 by subaerial alteration. The $fO_2$ of Mangaia lavas should be verified in fresh samples, which are
374 unfortunately rare on this ~20 Ma island.

375

376 *3.3. Oxygen fugacity does not correlate with isotopic composition*

377 There are no correlations between $fO_2$ and He-Sr-Nd-W-Os-Pb isotopic compositions when
378 OIB are taken together globally (**Figure 6**). When OIB are separated by mantle component (e.g.,
379 HIMU, EM1, EM2) or by plume location, few correlations exist. The $fO_2$ of geochemically
380 depleted OIB correlates positively with radiogenic $^{206,207,208}Pb/^{204}Pb$ and negatively with
381 radiogenic $^{187}Os/^{188}Os$; however, this trend is primarily controlled by Hawaiian lavas. In Canary,
382 $fO_2$ is positively correlated with $^{87}Sr/^{86}Sr$; this correlation is also present when all HIMU-type lavas
383 are grouped together. Global HIMU also has a negative correlation between $fO_2$ and $^{143}Nd/^{144}Nd$.
384 For Baffin Island lavas, only $^{207}Pb/^{204}Pb$ is correlated with $fO_2$. Summaries of the Pearson's tests
385 between $fO_2$ and each isotopic system, to visualize statistically significant correlations in the
386 current dataset, are given by location and by mantle component in **Supplementary Figure S8 and**
387 **S9,** respectively.

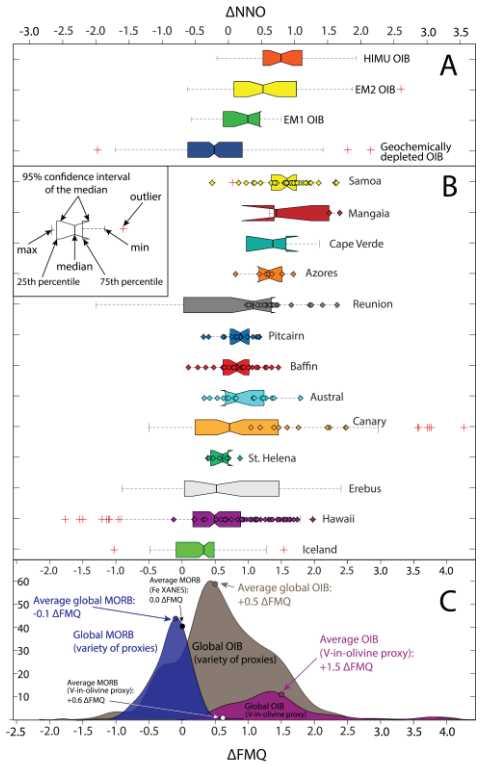


388

389 **Fig. 5.** Box and whisker plot illustrating the $fO_2$ distributions of lavas in this study (**Table 1**) and previously published
390 lavas (**Supplementary table S9**) grouped by mantle component **(A)** and by plume location **(B)**. All individual rock
391 data from this study only are superimposed as diamonds on top of each box. Data are considered outliers if they fall
392 outside of the "whiskers" defined by 1.5 × the interquartile range. Outliers in these plots are not excluded from
393 discussion or plots as they are considered real, high (or low) $fO_2$ recordings. Note that the top axis is $fO_2$ given as
394 ΔNNO and the bottom axis is ΔFMQ. Boxes are ordered by median $fO_2$. **(C)** Kernel probability density function for
395 global MORB (**Supplementary table S10**) compared to global OIB —including this study and the compiled dataset.
396 The purple distribution is the $fO_2$of OIB determined via the V-in-olivine proxy to illustrate that this method generally
397 produces higher $fO_2$ compared to other proxies.

398

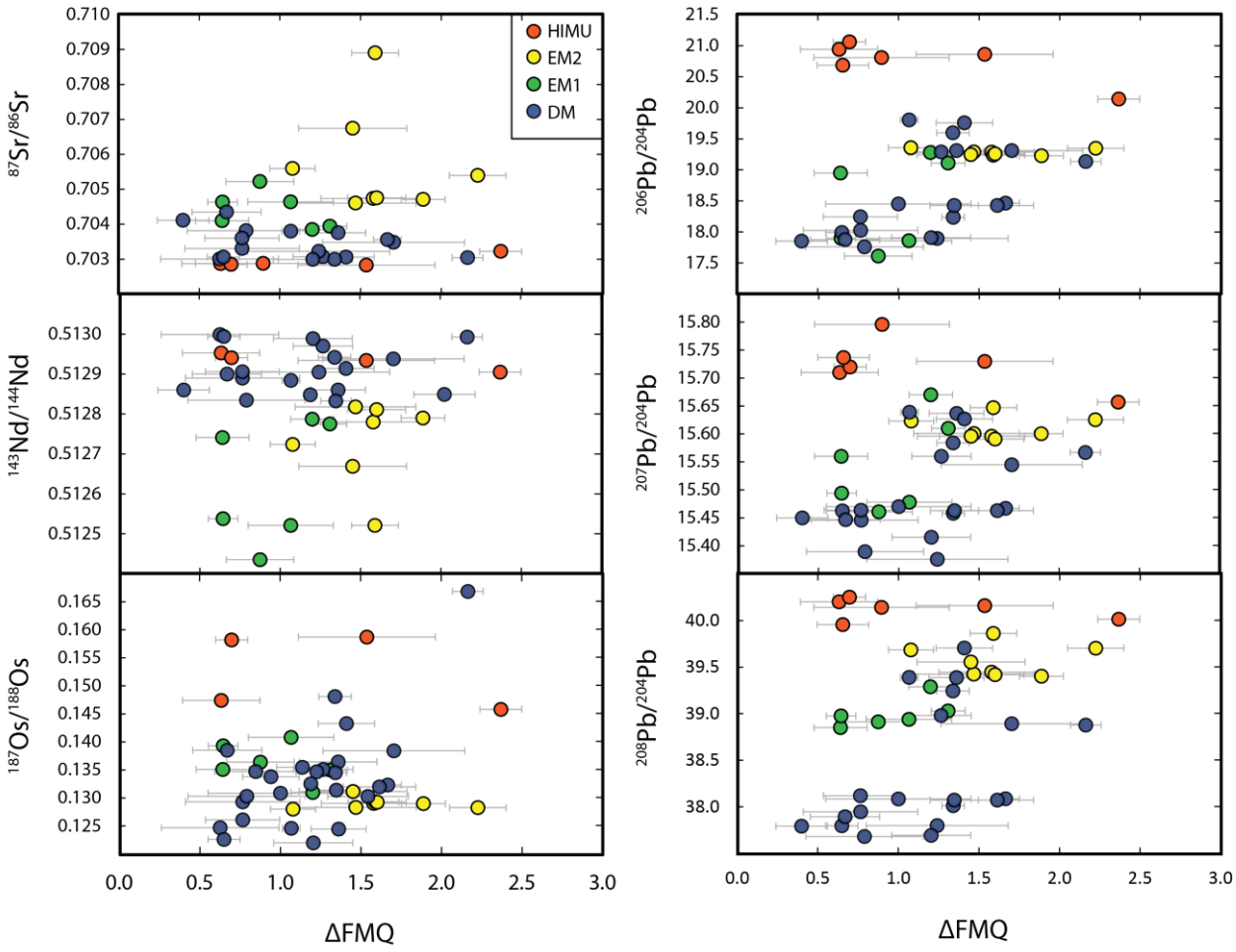


**Fig 6. Oxygen fugacity plotted against isotopic compositions for each mantle component.** See **Supplementary Data S7** for isotope compilation and references. Error bars represent the 1SD. Supplementary Figure S10 shows the same plots with data color coded by plume locality instead of mantle component.

### *3.4. Offset between $fO_2$ determined by different proxies*

Previous studies (e.g., Taracsák et al., 2022) have shown that the $fO_2$ values recorded by OIB via the $D_V^{ol/melt}$ proxy are higher than $fO_2$ determined by other techniques, such as X-ray absorption near edge structure (XANES) spectroscopic measurements of $Fe^{+3}/Fe^{T}$ and S speciation (**Figure 5C**). In the compiled global OIB database there are 509 previously published $fO_2$ data: 94 data are derived from $D_V^{ol/melt}$ and 390 data are calculated from XANES or micro-XANES measurements of $Fe^{+3}/Fe^{T}$ (**see Supplementary Table S9).** This study adds an additional 56 $fO_2$

412 measurements via the $D_V^{ol/melt}$ proxy. The average $fO_2$ observed in the data set presented here is
413 +1.2 ΔFMQ, similar to the average value for all OIB $fO_2$ measurements derived from $D_V^{ol/melt}$
414 systemics (i.e., +1.5 ΔFMQ; Nicklas et al., 2019; Nicklas et al., 2022; Taracsák et al., 2022). In
415 contrast, the average $fO_2$ determined in OIB via XANES and micro-XANES is +0.4 ΔFMQ
416 (Moussallam et al., 2014, 2016, 2019; Shorttle et al., 2015; Helz et al., 2017; Brounce et al., 2017,
417 2022; Hartley et al., 2017). Other techniques in the compilation ($n$ = 25)—including titrimetric
418 determination of $Fe^{2+}$, X-ray fluorescence for $Fe^T$, MgO thermogeobarometry, etc.—yield even
419 lower $fO_2$ with a average of +0.3 ΔFMQ.

420 The maximum estimates by XANES are generally in agreement with the $fO_2$ determined
421 using $D_V^{ol/melt}$. For example, using the 2SD of the average, the observed of $fO_2$ of Canary (2.5
422 ΔFMQ ± 2.0), Hawaii (1.2 ΔFMQ ± 0.8), and Reunion (1.1 ΔFMQ ± 1.1) determined by
423 $D_V^{ol/melt}$ overlap the maximum $fO_2$ observed using XANES for these localities (1.4, 2.0, and 0.08
424 ΔFMQ, respectively). The average $fO_2$ for lavas from Kilauea in this study (+1.5 ΔFMQ) is within
425 the range of $fO_2$ observations in the least degassed Kilauea melt inclusions and glasses (0.7 to 2.0
426 ΔFMQ), as determined by XANES (Moussallam et al., 2016; Helz et al., 2017). Sulfur degassing
427 at Kilauea reduces the residual melt; therefore, the maximum observed $fO_2$ may be closer to the
428 source composition (Moussallam et al., 2016, 2019; Humphreys et al., 2022). The olivines from
429 Kilauea in this study are more primitive (Fo# 86.3 to 90.5) compared to those that hosted the melt
430 inclusions examined via XANES (Fo# 77.5 to 82.5; (Moussallam et al., 2016). Earlier crystallizing
431 olivines are less affected by S degassing (which would serve to lower the magma $fO_2$ through the
432 loss of an oxidizing agent). Further, diffusive equilibration of $Fe^{3+}/\sum Fe$ in olivine-hosted melt
433 inclusions will create offset between the $fO_2$ that is "locked in" by the $D_V^{ol/melt}$ proxy (Humphreys
434 et al., 2022). The precision of the XANES method allows for tracking the evolution of $fO_2$ in the
435 melt system; paired XANES and $D_V^{ol/melt}$ observations provide greater context to the $fO_2$
436 systematics of OIB. The $fO_2$ observed in this study is closer to the maximum observed by XANES
437 in the least degassed samples (Moussallam et al., 2016; Helz et al., 2017; Humphreys et al., 2022).
438 For added context, a previous investigation of Canary Islands OIB using XANES on relatively
439 undegassed, olivine-hosted melt inclusions estimated a mantle source $fO_2$ of +2.0 ΔFMQ
440 (Moussallam et al., 2019), consistent with the average Canary $fO_2$ determined in this study (+1.8
441 ΔFMQ). Canary lavas in this study range from +1.4 to +2.4 ΔFMQ, which overlaps with Canary

lavas from other studies using the sample proxy ($D_V^{ol-melt}$) that range from +1.3 to +3.9 ΔFMQ (Taracsák et al., 2022; Nicklas et al., 2022b). Thus, differences between the range of $fO_2$ determined via $D_V^{ol/melt}$ systematics versus that derived from (micro-)XANES techniques may represent a sampling bias in which prior XANES work focused on samples with variable extents of degassing to understand the evolution of $fO_2$ during petrogenesis.

## 4 Discussion

### *4.1. Petrologic influence on calculated $fO_2$ in OIB*

While this study primarily aims to investigate the link between lithospheric recycling and mantle $fO_2$, it is critical to evaluate the effects of OIB petrogenesis and the influence of ancient mantle domains on $fO_2$ in global OIB. Oxygen fugacity is influenced by mantle potential temperature such that higher mantle potential temperatures produce lower $fO_2$ even with a fixed $Fe^{3+}/\sum Fe$ of the peridotite source (Gaetani, 2016). A difference in mantle potential temperatures among plume localities, and between plume and mid-ocean ridges, is unlikely to explain the variability observed in global OIB. First, $fO_2$ does not vary systematically with mantle potential temperature among plume localities; a negative correlation would be expected if mantle potential temperature was the main control of the average $fO_2$ of OIB (Supplementary Figure 11). Second, the mantle plumes localities studied here have mantle potential temperatures that are, on average, approximately 130 °C hotter than ridges (Bao et al., 2022). Hotter mantle potential temperautes at plumes would predict lower $fO_2$; however, typically the plumes studied here overlap or have higher $fO_2$ than MORB (Figure 5). The effect of mantle potential temperature, if any, is less than the uncertainties of the $fO_2$ observed in this study.

Whether partial melting influences the $fO_2$ determined by the $D_V^{ol-melt}$ proxy in global OIB requires consideration. Within any hotspot location, the calculated $fO_2$ does not vary systematically with MgO, $TiO_2$, or $Na_2O$ content of the parental melt (Supplementary Table S6), which are sensitive to melt degree. La/Sm and La/Yb, which are inversely correlated with degree of partial melting, do not vary systematically with $fO_2$ within individual hotspot locations. There is a weak relationship between La/Sm and $fO_2$ in the global dataset ($r^2 = 0.1$, p value <0.1). The absence of correlations between $fO_2$ and other incompatible major element composition (both whole rock and parental) and trace elements indicates degree of partial melting does not control the $fO_2$ determined

by $D_V^{ol-melt}$ within hotspot lavas. Therefore, the weak trend between $fO_2$ and La/Sm globally may instead be primarily related to source enrichment. If source enrichment has an effect on $fO_2$, the relationship between La/Sm and $fO_2$ may be attenuated by the modification of the source La/Sm due to fractionation of La and Sm during partial melting. The mechanisms and conditions of melting, as well as mineralogical differences, among OIB may be important in controlling the $fO_2$ of plume-derived melts; further work is needed to assess these effects in detail. Effects less than one log unit are difficult to ascertain in this study given the uncertainties when using the $D_V^{ol-melt}$ proxy in OIB.

The $CaO/Al_2O_3$ of the melt system remains relatively constant during olivine crystallization but decreases during pyroxene crystallization. Clinopyroxene (and orthopyroxene) generally has a higher $D_V^{mineral-melt}$ compared to olivine at the same $fO_2$ and temperature (Wang et al., 2019). Pyroxene fractionation after primitive olivine crystallization would remove V from the melt resulting in a higher measured $D_V^{ol-melt}$ (and therefore, lower calculated $fO_2$). A *negative* correlation between $fO_2$ and $CaO/Al_2O_3$ would provide evidence that the calculated $fO_2$ was affected by clinopyroxene fractionation. Within the dataset presented here, there are no global or local (i.e., within an individual plume locality) negative correlations between whole rock $CaO/Al_2O_3$ and $fO_2$. A detailed investigation of a greater number of cogenetic samples from each locality may better illuminate the effects of clinopyroxene fractionation on $fO_2$ determination using $D_V^{ol-melt}$. There is, however, a *positive* correlation between $CaO/Al_2O_3$ and $fO_2$ in the global dataset as well as within the Hawaiian and Canary plumes (e.g., Supplementary Figure S12). Within all Hawaiian lavas and within individual Hawaiian volcanic centers, there is no relationship between $CaO/Al_2O_3$ and MgO content. This suggests there is no significant effect from pyroxene fractionation in the Hawaiian lavas. Three of the four Canary lavas are described as ankaramites that derive from a pyroxenite-rich mantle source (Day et al., 2009). Therefore, rather than pyroxene fractionation during petrogenesis, the positive relationship between $CaO/Al_2O_3$ and $fO_2$ in OIB may be related to the plume source (e.g., carbonated recycled materials and/or pyroxenite), which is discussed below.

### *4.2. The role of lithospheric recycling in elevated OIB $fO_2$*

Subduction, accumulation, and redistribution of lithosphere in the Earth's mantle has been invoked to account for the chemical divergence between MORB—which are byproducts of

decompression melting of the upper mantle—and OIB that may sample mantle domains as deep as the core-mantle boundary (Gast, 1968; Morgan, 1971; Hofmann and White, 1982; Foley, 2011). It has been suggested that subduction of lithosphere leads to higher $fO_2$ in the mantle (Kasting et al., 1993; Lécuyer and Ricard, 1999; Evans, 2012; Brounce et al., 2019). It has been shown that subducted lithosphere retains the majority of its oxidized material during subduction (Brounce et al., 2019) and that a large mass of recycled lithosphere remains oxidized relative to ambient mantle at ≥300 km depth due to the survival of carbonates in carbonated eclogites (Yaxley and Green, 1994; Foley, 2011). Thus, recycled lithosphere in plume sources has been cited to explain observations of elevated $fO_2$ in OIB compared to global MORB (Moussallam et al., 2014, 2016, 2019; Shorttle et al., 2015; Helz et al., 2017; Brounce et al., 2017; Hartley et al., 2017; Taracsák et al., 2022; Nicklas et al., 2022b).

The offset between $fO_2$ observed in MORB and OIB may be attributed to oxidation of plume sources by lithosphere recycling. The influence of recycled material on the $fO_2$ of mantle-derived magmas is complicated; the addition of recycled material may increase *or* decrease the $fO_2$ of melt systems. For example, prior studies have shown that geochemical enrichment of MORB sources by addition of crustal sediments may serve to locally *lower* the $fO_2$ of enriched MORB (E-MORB), as evidenced by systematically lower $fO_2$ observed in E-MORB using XANES (Cottrell and Kelley, 2013). Reduced carbon from ancient anoxic ocean sediments leads to reduction of ferric iron during decompression melting and petrogenesis. The opposite is observed at the Reykjanes Ridge, where plume-influenced MORB become systematically oxidized and geochemically enriched as the ridge approaches mainland Iceland (Shorttle et al., 2015; Novella et al., 2020). The proximity of Reykjanes Ridge basalts to the Icelandic mantle plume suggests that the plume could be the source of higher $fO_2$ material; it has been interpreted that the oxidized component is entrained oceanic crust in the plume (Shorttle et al., 2015; Novella et al., 2020).

The two examples described above demonstrate that different crustal compositions can effectively reduce or oxidize the mantle sources. Ancient pelagic sediments, which contain abundant reduced carbon, may reduce the mantle while oceanic crust, which contains a greater proportion of ferric iron than ambient mantle, may be more likely to oxidize the ambient mantle. Since global OIB overlap MORB $fO_2$ but extend to much higher $fO_2$, lithospheric recycling does not reduce plume sources to a greater extent than MORB sources as no known OIB have lower

531 $fO_2$ than MORB. Lithospheric recycling may oxidize plume sources to a greater extent than is
532 observed in the MORB mantle, perhaps because the proportion and/or chemical compositions of
533 lithospheric material added to plume sources after subduction are distinct from recycled material
534 in the shallower MORB mantle.

535 Mantle components, which are thought to result in part from recycling of different types of
536 lithospheric material, provide an opportunity to test whether different types of recycled materials
537 cause net oxidation or reduction in plume sources. For example, EM1 lavas have been speculated
538 to contain recycled oceanic crust with pelagic sediment from the seafloor or delaminated lower
539 continental crust (McKenzie and O'Nions, 1983; Weaver, 1991; Garapić et al., 2015). The EM2
540 lavas have isotopic and trace element signatures consistent with a contribution of recycled
541 terrigenous sediment or metasomatized lithosphere (Workman et al., 2004; Jackson et al., 2007).
542 HIMU lavas are often attributed to recycling of a chemically-modified oceanic crustal package
543 such as carbonated eclogite (Hofmann, 1997; Moreira and Kurz, 2001; Stracke et al., 2005;
544 Dasgupta et al., 2007). Ocean island basalts that are geochemically depleted generally lack
545 observable signatures from lithospheric recycling and are likely the least chemically modified by
546 recycling compared to other OIB. Lavas in this study are grouped into these mantle components
547 based on their isotopic compositions (see **Section 2.7.**). We investigated the $fO_2$ systematics of
548 each group.

549 *4.2.1. HIMU lavas*

550 In the global suite presented here, HIMU has the highest and most variable $fO_2$. The
551 average HIMU $fO_2$ (1.5 ± 3.0 ΔFMQ) is statistically higher than both enriched mantle types, as
552 well as the geochemically depleted lavas (**Figure 5**). HIMU lavas also host olivine with the greatest
553 CaO wt. % and whole-rocks with the highest $CaO/Al_2O_3$ (**Figure 4; Supplementary Figure S12**).
554 The addition of volatile, oxidizing agents, like $C^{4+}$ and $S^{6+}$, in subducted carbonated lithosphere
555 has been invoked to account for the highly oxidized and volatile-rich HIMU lavas in El Hierro,
556 Canary (Taracsák et al., 2022). Reduction of carbonate and sulfate will lead to oxidation of silicates
557 as observed in arc settings (Rielli et al., 2017). Recycled, carbonated oceanic crustal materials in
558 the HIMU source can explain the radiogenic Pb isotopic compositions and elevated $CaO/Al_2O_3$ of
559 HIMU-type lavas (Dasgupta et al., 2007; Jackson and Dasgupta, 2008). Relatively high olivine
560 CaO wt. % has been previously argued to reflect carbonatitic metasomatism in the HIMU source

(Weiss et al., 2016). Our global dataset supports recycling of carbonated materials, such as oceanic crust in the form pyroxenite, to produce elevated $fO_2$, $CaO/Al_2O_3$, and olivine CaO content in HIMU-type OIB. HIMU lavas show a positive correlation between $fO_2$ and $^{87}Sr/^{86}Sr$ and negative correlation with $^{143}Nd/^{144}Nd$, which supports the existence of a geochemically-enriched, high $fO_2$ end-member in the plume source; however, there is no reason that a carbonated component would necessarily produce a correlation with $^{143}Nd/^{144}Nd$. High La/Sm, associated with higher $fO_2$ (**Section 4.1**) in OIB, likely points to the link between material with long-term geochemical enrichment (like recycled oceanic or continental crust) and high $fO_2$. Variations in Fe and C content and speciation in the subducting slab, as well as subduction environment and timing of recycling, likely play a role in decoupling $fO_2$ from tracers of recycled materials and creating scatter in the observed dataset.

HIMU lavas from St. Helena are distinctly less oxidized than HIMU lavas from the Macdonald (including Mangaia and Austral lavas) and Canary hotspots. Distinct $fO_2$ observed in St. Helena compared to other HIMU lavas may reflect a different composition of recycled material in the St. Helena plume source; however, high whole-rock $CaO/Al_2O_3$ and olivine CaO content are observed in St. Helena lavas. Heavy Zn isotopic compositions, which are linked to recycled surficial carbonates, are observed in St. Helena and other HIMU-type lavas (Zhang et al., 2022). These observations support a carbonated recycled crust in the St. Helena plume source, so it is unclear why St. Helena lavas in this study are among the lowest $fO_2$ in the global dataset (**Figure 5**). Complex subduction processes affect the redox potential of subducting material and may also decouple $fO_2$ from time-integrated radiogenic isotopic compositions. For example, partial melting during subduction could reduce the $Fe^{3+}/Fe_{tot}$ and C content of the subducting slab before it is entrained in a mantle plume.

*4.2.2. Enriched mantle (EM1 and EM2) OIB*

Previous studies of $fO_2$ in geochemically-enriched OIB have considered EM1 and EM2 lavas together (Nicklas et al., 2022b). Here, the $fO_2$ of EM1-type and EM2-type lavas are considered separately for the first time. The EM1 lavas (average = 0.2 ± 0.6 ΔFMQ) have statistically lower $fO_2$ than HIMU but are not distinct from EM2 or geochemically depleted OIB (**Figure 5**). The EM1 type of recycled material, likely recycled pelagic sediments based on their high Th/U and Lu/Hf required to explain the time-integrated Nd, Hf, Pb isotopic compositions of

EM1, may not have the potential to significantly oxidize the mantle source despite imparting radiogenic $^{87}Sr/^{86}Sr$ on the lavas. As discussed earlier, sediments can lower mantle $fO_2$ depending on their depositional environment (Cottrell and Kelley, 2013).

EM2 OIB (average = 0.7 ± 0.7 ΔFMQ) are oxidized relative to geochemically depleted OIB (average = -0.3 ± 1.1 ΔFMQ) but less so than HIMU. Though continental sediments have been invoked to account for the radiogenic $^{87}Sr/^{86}Sr$ signatures of EM2-type lavas, recycled sediments do not contribute as much to the net redox budget of recycle material compared altered oceanic crust and serpentinized lithosphere (e.g., Evans, 2012). Continentally-derived sediments may be present in EM2 plumes but might not have the capacity to drive oxidation of the mantle source. Recycled lithosphere that has been metasomatized by carbonatitic fluids can also account for the isotopic signatures of EM2 lavas in Samoa (Hauri et al., 1993; Workman et al., 2004). Like HIMU-type lavas, EM2-type OIB generally exhibit higher $CaO/Al_2O_3$ and olivine CaO content than EM1 or geochemically depleted OIB (**Figure 4).** These chemical characteristics are similar to HIMU-type lavas and could result from carbonatite metasomatism in their mantle source or recycling of carbonated pyroxenite (Canil et al., 1994; Jackson and Dasgupta, 2008; Weiss et al., 2016). Despite few correlations between $fO_2$ and radiogenic isotopic compositions, there are statistical $fO_2$ distinctions among lavas linked to different mantle components. Decoupling of $fO_2$ and lithophile isotopic systems may occur during shallow plume dynamics such as the separation and rapid ascent of carbonatite or volatile-rich fluids relative to the silicate plume that carries lithophile trace elements (Valbracht et al., 1996; Hammouda and Laporte, 2000). If carbonated recycled material increases the $fO_2$ of plume sources, then preferential melting of high $fO_2$ carbonatite or $CO_2$-rich fluid in the shallow plume may cause physical separatation from the lithophile trace elements in silicate that link to lithospheric recycling (Valbracht et al., 1996; Hammouda and Laporte, 2000; Hofmann et al., 2011).

### *4.2.3 Depleted mantle OIB*

Depleted mantle OIB extend to the most reducing conditions and overlap with MORB $fO_2$. These lavas exhibit robust positive correlations between $fO_2$ and $^{206}Pb/^{204}Pb$, $^{207}Pb/^{204}Pb$, and $^{208}Pb/^{204}Pb$, as well as negative correlation between $fO_2$ and $^{187}Os/^{188}Os$. However, these relationships are primarily controlled by Hawaiian lavas (Supplementary **Figure S10**). Radiogenic

Os and unradiogenic Pb in Ko'olau has been associated with recycled pelagic sediment that may have experienced U loss in oxidized marine environments (Lassiter and Hauri, 1998). The pelagic sediment signature trends toward lower $fO_2$, which suggests that pelagic sediment reduces the plume source with a similar mechanism to that observed in E-MORB (Cottrell and Kelley, 2013).

Another recycling model has been suggested to explain the major element and lithophile isotopic compositions of Ko'olau lavas: the Ko'olau source may contain greater proportion of recycled eclogite compared to Kīlauea and Hualālai (Hauri, 1996). Archean eclogites are reducing compared to the modern mantle (Aulbach et al., 2019), and if present as recycled material in the Ko'olau mantle source, could lower the $fO_2$ in Ko'olau lavas relative to Kīlauea and Hualālai.

The spatio-temporal trend towards higher $fO_2$ from Ko'olau to Hualālai and Kīlauea (**Figure 7**) may also reflect the introduction of an oxidized component, such as hydrothermally-altered lower oceanic crust or lithospheric mantle to the Hawaiian plume. Considering Hawaiian lavas extend to higher $fO_2$ than MORB, a relatively oxidized component is required to explain $fO_2$ up to +1.7 ΔFMQ (**Figure 5**). Multiple processes and recycled materials may be at play in the Hawaiian plume to explain the range of $fO_2$ observed.

An inverse correlation between $fO_2$ and $^{207}Pb/^{204}Pb$ in Baffin Island is opposite to the positive trend observed in Hawaii (Supplementary **Figure S10)**. Geochemically depleted isotopic signatures (i.e., low $^{87}Sr/^{86}Sr$ and high $^{143}Nd/^{144}Nd$) along with MORB-like $^{187}Os/^{188}Os$ in Baffin lavas can be attributed to a depleted mantle source that does not contain significant contributions from recycled materials. Further, since only $^{207}Pb/^{204}Pb$ correlates significantly with $fO_2$, and not $^{206}Pb/^{204}Pb$, $^{208}Pb/^{204}Pb$, or any other radiogenic isotope system in this study, lithospheric recycling does not explain the variability in $fO_2$ of Baffin Island lavas.

Baffin Island is unique in the global suite because the plume lavas erupted through Archean and paleo-Proterozoic continental crust (Saunders et al., 2013). Using Nb/Th and Ce/Pb as identifiers of crustal assimilation (e.g., Willhite et al., 2019), where low Nb/Th (<13) and low Ce/Pb (<20) are indicative of crustal assimilation, all of the Baffin Island lavas in this study have been at least moderately affected by crustal contamination (**Supplementary Figure S13**). However, crustal contamination does not appear to have modified the oxygen fugacity of the Baffin lavas as there is no significant correlation between $fO_2$ and Nb/Th, Ce/Pb, or $^{87}Sr/^{86}Sr$, $^{206}Pb/^{204}Pb$, $^{208}Pb/^{204}Pb$, etc. The two lavas with the lowest Ce/Pb are offset to higher $fO_2$; however,

650 those two samples have the *highest* Nb/Th, which is inconsistent with crustal assimilation. Thus,
651 the Pb-$fO_2$ trend observed in Baffin does not likely reflect lithospheric recycling or crustal
652 assimilation.

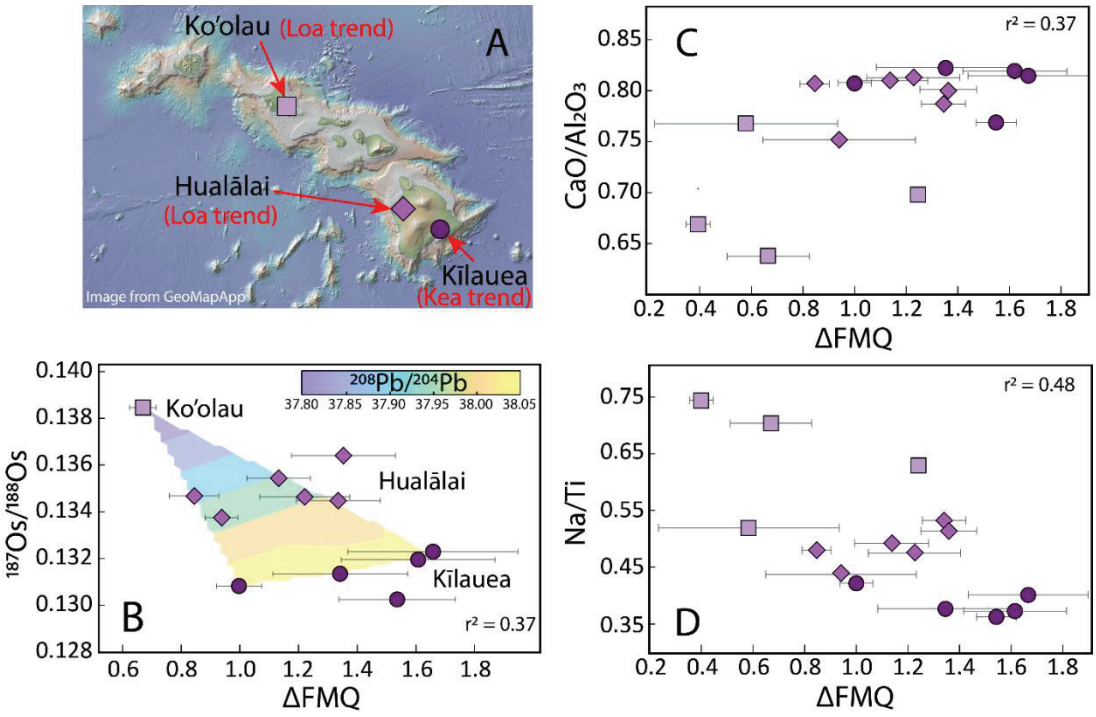


653

654 **Fig 7. (A)** Bathymetry map made using GeoMapApp (www.geomapapp.org) showing the three volcanic centers that
655 have new $fO_2$ data presented in this study. (**B**) Osmium isotopic compositions of the Hawaiian lavas in this study
656 negatively correlate with $fO_2$ ($r^2 = 0.37$), whereas $^{206,207,208}Pb/^{204}Pb$ positively correlate with $fO_2$ ($r^2 = 0.76$, 0.51, 0.77,
657 respectively). The colored contours reflect a linear interpolation among $^{208}Pb/^{204}Pb$ data. There is also a spatio-
658 temporal trend with increasing $fO_2$ and $^{206,207,208}Pb/^{204}Pb$ and decreasing $^{187}Os/^{188}Os$ from Ko'olau (oldest) to Kīlauea
659 (youngest). (**C**) CaO/Al2O3 and (**D**) Na/Ti of Hawaiian whole-rocks have robust correlations (i.e., Pearson's
660 correlation coefficient has a p value <0.1) with $fO_2$.

661

662 *4.3. Influence from ancient and/or core-equilibrated mantle domains?*

663 Helium and tungsten isotopes in plume-derived lavas have been used to identify
664 contributions from one or more ancient, well-preserved and/or core equilibrated reservoir(s) in the
665 lower mantle (Hart et al., 1992; Class and Goldstein, 2005; Rizo et al., 2016; Mundl et al., 2017).
666 Lavas with elevated $^3He/^4He$ compared to typical MORB ($^3He/^4He$ = 6-10 Ra; where Ra denotes
667 the sample's measured $^3He/^4He$ relative to Earth's atmospheric $^3He/^4He$) sample an ancient
668 reservoir that has been partially or wholly preserved through geologic time (Kurz et al., 1982).

Discovery of $\mu^{182}W$ anomalies in plume-derived lavas (Mundl et al., 2017), as well as a correlation between $\mu^{182}W$ and $^{3}He/^{4}He$ in deep-rooted plumes (Mundl et al., 2017; Mundl-Petermeier et al., 2020), provide evidence for preservation of Earth reservoirs created in the early Hadean while $^{182}Hf$ was extant (i.e., within ~60 My of Solar System formation). OIB with the highest $^{3}He/^{4}He$ and greatest magnitude $\mu^{182}W$ anomalies also appear to the least modified by addition of recycled materials (Jackson et al., 2020). If the $fO_2$ of ancient/core-equilibrated plume reservoirs are distinct from the modern convecting mantle, then $fO_2$ may be coupled with high $^{3}He/^{4}He$, anomalous $\mu^{182}W$, and a low $D^{Sr\text{-}Nd\text{-}Pb}$ (a parameter that generally increases with the amount of recycled material entrained in a plume; Jackson et al., 2020). Given that $fO_2$ generally does not correlate with radiogenic isotope indicators of recycled material, it is plausible that plumes have heterogeneous and elevated $fO_2$ due to interaction with an ancient and/or core-equilibrated reservoir.

For all lavas with published He and/or W isotopes in this study, there is no statistically significant correlation with $fO_2$ (**Figure 8)**; however, high $^{3}He/^{4}He$ lavas are limited in this dataset, and only ten lavas have $^{3}He/^{4}He$ above 10 Ra. In previous studies of noble gas systematics in OIB, all studied OIB had higher $fO_2$ than MORB, regardless of $^{3}He/^{4}He$ (Day et al., 2022). Typically, OIB with a higher proportion of recycled material (i.e., a greater $D^{Sr\text{-}Nd\text{-}Pb}$), fall along mixing lines between MORB and various recycled end members with higher $Fe^{3+}/\sum Fe$ (Brounce et al., 2020). This inidicates that OIB with less recycled material do not have inherently higher $fO_2$ than other OIB and MORB. Given the limited number of samples with paired $fO_2$ and elevated $^{3}He/^{4}He$ measurements or anomalous $\mu^{182}W$, a critical evaluation of the $fO_2$ of OIB with those signatures may still be warranted in future studies. It is not apparent that ancient and/or core-equilibrated mantle, sampled by some OIB, has distinct $fO_2$ from the ambient mantle or that the $fO_2$ of the deep mantle source would be preserved once entrained in a mantle plume. This demonstrates that the offset to higher $fO_2$ observed in OIB is not likely related to the mechanism(s) that produce and preserve high $^{3}He/^{4}He$ and anomalous $\mu^{182}W$.

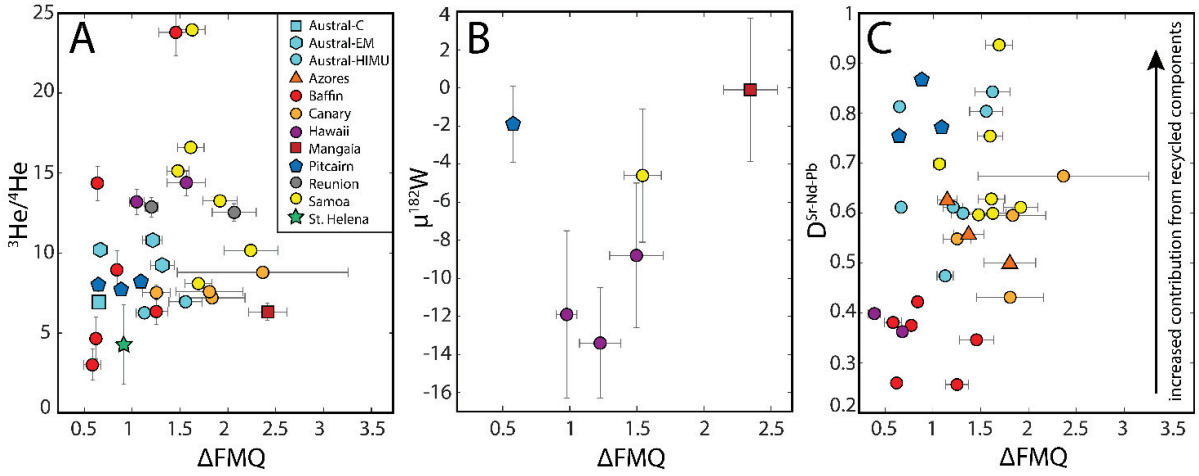


**Fig 8. Ancient geochemical signals, such as high $^3He/^4He$ (A) and anomalous $\mu^{182}W$ (B), do not correlate with $fO_2$.** Vertical error bars are 2SD (internal) for helium isotopes and 2SE (internal) for tungsten isotopes. **(C)** Increasing $D^{Sr\text{-}Nd\text{-}Pb}$ reflects a larger proportion of recycled material in the source (Jackson et al., 2020). Lavas with the lowest $D^{Sr\text{-}Nd\text{-}Pb}$ should represent mantle sources least affected by lithospheric recycling.

## 5 Conclusions

We provide $fO_2$ constraints for lavas derived from key mantle components (EM1, EM2, HIMU, geochemically depleted OIB) in a global framework to characterize global OIB using the same analytical techniques across our dataset. We also provide a database of previously published MORB and OIB $fO_2$ from a variety of techniques and $fO_2$ proxies for cross-comparison. We find that $\boldsymbol{D_V^{ol/melt}}$ results in higher $fO_2$ than $Fe^{3+}/Fe^T$ and other oxybarometers, perhaps due to degassing-related phenomena during progressive melt differentiation. Though few robust correlations exist between radiogenic isotope compositions and $fO2$, lithospheric recycling remains a viable mechanism for the oxidation of plume source regions in the mantle. Despite overlap among HIMU, EM2, EM1, and depleted OIB, ANOVA tests reveal that HIMU- and EM2-type OIB are distinctly oxidized compared to depleted OIB , Given that these lavas contain isotopic and petrologic evidence for carbonate-related crustal recycling. Even geochemically depleted OIB with limited evidence of lithospheric recycling, such as Hawaiian lavas, show evidence for a geochemically-enriched, oxidized component in their plume source. So far, there is limited evidence that primitive geochemical signals like elevated $^3He/^4He$ or negative $\mu^{182}W$

715 are associated with distinct $fO_2$. These findings support the link between lithospheric recycling
716 tectonics and variable and elevated $fO_2$ in Earth's interior.

717
718
719 **Acknowledgments**
720 We would like to acknowledge funding from the NASA ROSES Program Grant#
721 80NSSC19K0768 and NSF EAR Grant #1944552.The authors would like to thank Frank Spera,
722 Richard Ash, and James Dottin III for helpful discussion. Thank you to Maddy Raith, who
723 helped make scans of the epoxy-mounted samples and helped with compilation of global MORB
724 $fO_2$ data. Reviewers of this version and a previous version of this manuscript helped improve this
725 work, including Maryjo Brounce and anonymous reviewers.
726
727 **Open Research**

728 The new $fO_2$ data and all compiled data used for investigating the $fO_2$, petrologic, and isotopic
729 compositions of global ocean island basalts in the study are available in the EarthChem Library
730 at https://doi.org/10.26022/IEDA/113038.
731

732 **References**

733 Andrault D., Muñoz M., Pesce G., Cerantola V., Chumakov A., Kantor I., Pascarelli S., Rüffer R. and
734 Hennet L. (2018) Large oxygen excess in the primitive mantle could be the source of the Great
735 Oxygenation Event. *Geochem. Persp. Let.*, 5–10.

736 Aulbach S., Woodland A. B., Stern R. A., Vasilyev P., Heaman L. M. and Viljoen K. S. (2019) Evidence for a
737 dominantly reducing Archaean ambient mantle from two redox proxies, and low oxygen fugacity
738 of deeply subducted oceanic crust. *Sci Rep* **9**, 20190.

739 Bao X., Lithgow-Bertelloni C. R., Jackson M. G. and Romanowicz B. (2022) On the relative temperatures
740 of Earth's volcanic hotspots and mid-ocean ridges. *Science* **375**, 57–61.

741 Borisov A. A., Kadik A. A., Zharkova Y. V. and Kalinichenco N. V. (1987) Effects of oxygen fugacity on the
742 ratio between valency forms of vanadium in magmas. *Geochemistry International* **24**, 15–20.

743 Brounce M., Cottrell E. and Kelley K. A. (2019) The redox budget of the Mariana subduction zone. *Earth
744 and Planetary Science Letters* **528**, 115859.

745 Brounce M., Stolper E. and Eiler J. (2017) Redox variations in Mauna Kea lavas, the oxygen fugacity of
746 the Hawaiian plume, and the role of volcanic gases in Earth's oxygenation. *PNAS* **114**, 8997–9002.

747 Brounce M., Stolper E. and Eiler J. (2022) The mantle source of basalts from Reunion Island is not more
748 oxidized than the MORB source mantle. *Contrib Mineral Petrol* **177**, 7.

749 Canil D. (1997) Vanadium partitioning and the oxidation state of Archaean komatiite magmas. *Nature*
750 **389**, 842–845.

751 Canil D. (1999) Vanadium partitioning between orthopyroxene, spinel and silicate melt and the redox
752 states of mantle source regions for primary magmas. *Geochimica et Cosmochimica Acta* **63**, 557–
753 572.

754 Canil D. and Fedortchouk Y. (2001) Olivine–Liquid Partitioning of Vanadium and Other Trace Elements,
755 with Applications to Modern and Ancient Picrites. *The Canadian Mineralogist* **39**, 319–330.

756 Canil D., O'Neill H. St. C., Pearson D. G., Rudnick R. L., McDonough W. F. and Carswell D. A. (1994) Ferric
757 iron in peridotites and mantle oxidation states. *Earth and Planetary Science Letters* **123**, 205–220.

758 Class C. and Goldstein S. L. (2005) Evolution of helium isotopes in the Earth's mantle. *Nature* **436**, 1107.

759 Cockell C. s., Bush T., Bryce C., Direito S., Fox-Powell M., Harrison J. p., Lammer H., Landenmark H.,
760 Martin-Torres J., Nicholson N., Noack L., O'Malley-James J., Payler S. j., Rushby A., Samuels T.,
761 Schwendner P., Wadsworth J. and Zorzano M. p. (2016) Habitability: A Review. *Astrobiology* **16**,
762 89–117.

763 Condie K. C. (1976) *Plate Tectonics & Crustal Evolution*., Pergamon Press.

764 Cottrell E. and Kelley K. A. (2013) Redox Heterogeneity in Mid-Ocean Ridge Basalts as a Function of
765 Mantle Source. *Science* **340**, 1314–1317.

766 Danyushevsky L. V. and Plechov P. (2011) Petrolog3: Integrated software for modeling crystallization
767 processes. *Geochemistry, Geophysics, Geosystems* **12**.

768 Dasgupta R., Hirschmann M. M. and Smith N. D. (2007) Partial Melting Experiments of Peridotite + CO2
769 at 3 GPa and Genesis of Alkalic Ocean Island Basalts. *Journal of Petrology* **48**, 2093–2124.

770 Day J. M. D., Jones T. D. and Nicklas R. W. (2022) Mantle sources of ocean islands basalts revealed from
771 noble gas isotope systematics. *Chemical Geology* **587**, 120626.

772 Day J. M. D., Pearson D. G., Macpherson C. G., Lowry D. and Carracedo J.-C. (2009) Pyroxenite-rich
773 mantle formed by recycled oceanic lithosphere: Oxygen-osmium isotope evidence from Canary
774 Island lavas. *Geology* **37**, 555–558.

775 Evans K. A. (2012) The redox budget of subduction zones. *Earth-Science Reviews* **113**, 11–32.

776 Farley K. A., Natland J. H. and Craig H. (1992) Binary mixing of enriched and undegassed (primitive?)
777 mantle components (He, Sr, Nd, Pb) in Samoan lavas. *Earth and Planetary Science Letters* **111**,
778 183–199.

779 Foley S. F. (2011) A Reappraisal of Redox Melting in the Earth's Mantle as a Function of Tectonic Setting
780 and Time. *Journal of Petrology* **52**, 1363–1391.

781 French B. M. (1966) Some geological implications of equilibrium between graphite and a C-H-O gas
782 phase at high temperatures and pressures. *Reviews of Geophysics* **4**, 223–253.

783 Gaetani G. A. (2016) The behavior of Fe3+/∑Fe during partial melting of spinel lherzolite. *Geochimica et*
784 *Cosmochimica Acta* **185**, 64–77.

785 Gaetani G. A. and Grove T. L. (1997) Partitioning of moderately siderophile elements among olivine,
786 silicate melt, and sulfide melt: Constraints on core formation in the Earth and Mars. *Geochimica et*
787 *Cosmochimica Acta* **61**, 1829–1846.

788 Garapić G., Jackson M. G., Hauri E. H., Hart S. R., Farley K. A., Blusztajn J. S. and Woodhead J. D. (2015) A
789 radiogenic isotopic (He-Sr-Nd-Pb-Os) study of lavas from the Pitcairn hotspot: Implications for the
790 origin of EM-1 (enriched mantle 1). *Lithos* **228–229**, 1–11.

791 Gast P. W. (1968) Trace element fractionation and the origin of tholeiitic and alkaline magma types.
792 *Geochimica et Cosmochimica Acta* **32**, 1057–1086.

793 Hammouda T. and Laporte D. (2000) Ultrafast mantle impregnation by carbonatite melts. *Geology* **28**,
794 283–285.

795 Hart S. R., Hauri E. H., Oschmann L. A. and Whitehead J. A. (1992) Mantle Plumes and Entrainment:
796 Isotopic Evidence. *Science* **256**, 517–520.

797 Hartley M. E., Shorttle O., Maclennan J., Moussallam Y. and Edmonds M. (2017) Olivine-hosted melt
798 inclusions as an archive of redox heterogeneity in magmatic systems. *Earth and Planetary Science*
799 *Letters* **479**, 192–205.

800 Hauri E. H. (1996) Major-element variability in the Hawaiian mantle plume. *Nature* **382**, 415–419.

801 Hauri E. H., Shimizu N., Dieu J. J. and Hart S. R. (1993) Evidence for hotspot-related carbonatite
802 metasomatism in the oceanic upper mantle. *Nature* **365**, 221–227.

803 Helz R. T., Cottrell E., Brounce M. N. and Kelley K. A. (2017) Olivine-melt relationships and syneruptive
804 redox variations in the 1959 eruption of Kīlauea Volcano as revealed by XANES. *Journal of*
805 *Volcanology and Geothermal Research* **333–334**, 1–14.

806 Hirschmann M. M. (2012) Magma ocean influence on early atmosphere mass and composition. *Earth*
807 *and Planetary Science Letters* **341–344**, 48–57.

808 Hofmann A. W. (1997) Mantle geochemistry: the message from oceanic volcanism. *Nature* **385**, 219–
809 229.

810 Hofmann A. W., Farnetani C. G., Spiegelman M. and Class C. (2011) Displaced helium and carbon in the
811 Hawaiian plume. *Earth and Planetary Science Letters* **312**, 226–236.

812 Hofmann A. W. and White W. M. (1982) Mantle plumes from ancient oceanic crust. *Earth and Planetary*
813 *Science Letters* **57**, 421–436.

814 Humphreys J., Brounce M. and Walowski K. (2022) Diffusive equilibration of H2O and oxygen fugacity in
815 natural olivine-hosted melt inclusions. *Earth and Planetary Science Letters* **584**, 117409.

816 Jackson M. G., Becker T. W. and Konter J. G. (2018) Evidence for a deep mantle source for EM and HIMU
817 domains from integrated geochemical and geophysical constraints. *Earth and Planetary Science*
818 *Letters* **484**, 154–167.

Jackson M. G., Blichert-Toft J., Halldórsson S. A., Mundl-Petermeier A., Bizimis M., Kurz M. D., Price A. A., Harðardóttir S., Willhite L. N., Breddam K., Becker T. W. and Fischer R. A. (2020) Ancient helium and tungsten isotopic signatures preserved in mantle domains least modified by crustal recycling. *PNAS* **117**, 30993–31001.

Jackson M. G. and Dasgupta R. (2008) Compositions of HIMU, EM1, and EM2 from global trends between radiogenic isotopes and major elements in ocean island basalts. *Earth and Planetary Science Letters* **276**, 175–186.

Jackson M. G., Hart S. R., Koppers A. A. P., Staudigel H., Konter J., Blusztajn J., Kurz M. and Russell J. A. (2007) The return of subducted continental crust in Samoan lavas. *Nature* **448**, 684–687.

Kadoya S., Catling D. C., Nicklas R. W., Puchtel I. S. and Anbar A. D. (2020) Mantle data imply a decline of oxidizable volcanic gases could have triggered the Great Oxidation. *Nat Commun* **11**, 2774.

Kasting J. F., Eggler D. H. and Raeburn S. P. (1993) Mantle Redox Evolution and the Oxidation State of the Archean Atmosphere. *The Journal of Geology* **101**, 245–257.

Kump L. R., Kasting J. F. and Barley M. E. (2001) Rise of atmospheric oxygen and the "upside-down" Archean mantle. *Geochemistry, Geophysics, Geosystems* **2**.

Kurz M. D., Jenkins W. J. and Hart S. R. (1982) Helium isotopic systematics of oceanic islands and mantle heterogeneity. *Nature* **297**, 43–47.

Lassiter J. C. and Hauri E. H. (1998) Osmium-isotope variations in Hawaiian lavas: evidence for recycled oceanic lithosphere in the Hawaiian plume. *Earth and Planetary Science Letters* **164**, 483–496.

Lécuyer C. and Ricard Y. (1999) Long-term fluxes and budget of ferric iron: implication for the redox states of the Earth's mantle and atmosphere. *Earth and Planetary Science Letters* **165**, 197–211.

Locmelis M., Arevalo R. D., Puchtel I. S., Fiorentini M. L. and Nisbet E. G. (2019) Transition metals in komatiitic olivine: Proxies for mantle composition, redox conditions, and sulfide mineralization potential. *American Mineralogist* **104**, 1143–1155.

Mallmann G. and O'Neill H. St. C. (2013) Calibration of an Empirical Thermometer and Oxybarometer based on the Partitioning of Sc, Y and V between Olivine and Silicate Melt. *Journal of Petrology* **54**, 933–949.

Mallmann G. and O'Neill H. St. C. (2009) The Crystal/Melt Partitioning of V during Mantle Melting as a Function of Oxygen Fugacity Compared with some other Elements (Al, P, Ca, Sc, Ti, Cr, Fe, Ga, Y, Zr and Nb). *Journal of Petrology* **50**, 1765–1794.

McKenzie D. and O'Nions R. K. (1983) Mantle reservoirs and ocean island basalts. *Nature* **301**, 229–231.

Moreira M. and Kurz M. D. (2001) Subducted oceanic lithosphere and the origin of the 'high μ' basalt helium isotopic signature. *Earth and Planetary Science Letters* **189**, 49–57.

Morgan W. J. (1971) Convection Plumes in the Lower Mantle. *Nature* **230**, 42–43.

Moussallam Y., Edmonds M., Scaillet B., Peters N., Gennaro E., Sides I. and Oppenheimer C. (2016) The impact of degassing on the oxidation state of basaltic magmas: A case study of Kīlauea volcano. *Earth and Planetary Science Letters* **450**, 317–325.

Moussallam Y., Longpré M.-A., McCammon C., Gomez-Ulla A., Rose-Koga E. F., Scaillet B., Peters N., Gennaro E., Paris R. and Oppenheimer C. (2019) Mantle plumes are oxidised. *Earth and Planetary Science Letters* **527**, 115798.

Moussallam Y., Oppenheimer C., Scaillet B., Gaillard F., Kyle P., Peters N., Hartley M., Berlo K. and Donovan A. (2014) Tracking the changing oxidation state of Erebus magmas, from mantle to surface, driven by magma ascent and degassing. *Earth and Planetary Science Letters* **393**, 200–209.

Mundl A., Touboul M., Jackson M. G., Day J. M. D., Kurz M. D., Lekic V., Helz R. T. and Walker R. J. (2017) Tungsten-182 heterogeneity in modern ocean island basalts. *Science* **356**, 66–69.

Mundl-Petermeier A., Walker R. J., Fischer R. A., Lekic V., Jackson M. G. and Kurz M. D. (2020) Anomalous 182W in high 3He/4He ocean island basalts: Fingerprints of Earth's core? *Geochimica et Cosmochimica Acta* **271**, 194–211.

Nicklas R. W., Hahn R. K. M. and Day J. M. D. (2022a) Oxidation of La Réunion lavas with MORB-like fO2 by assimilation. *Geochemical Perspectives Letters*.

Nicklas R. W., Hahn R. K. M., Willhite L. N., Jackson M. G., Zanon V., Arevalo R. and Day J. M. D. (2022b) Oxidized mantle sources of HIMU- and EM-type Ocean Island Basalts. *Chemical Geology* **602**, 120901.

Nicklas R. W., Puchtel I. S., Ash R. D., Piccoli P. M., Hanski E., Nisbet E. G., Waterton P., Pearson D. G. and Anbar A. D. (2019) Secular mantle oxidation across the Archean-Proterozoic boundary: Evidence from V partitioning in komatiites and picrites. *Geochimica et Cosmochimica Acta* **250**, 49–75.

Novella D., Maclennan J., Shorttle O., Prytulak J. and Murton B. J. (2020) A multi-proxy investigation of mantle oxygen fugacity along the Reykjanes Ridge. *Earth and Planetary Science Letters* **531**, 115973.

O'Neill C. and Aulbach S. (2022) Destabilization of deep oxidized mantle drove the Great Oxidation Event. *Science Advances* **8**, eabg1626.

Ortenzi G., Noack L., Sohl F., Guimond C. M., Grenfell J. L., Dorn C., Schmidt J. M., Vulpius S., Katyal N., Kitzmann D. and Rauer H. (2020) Mantle redox state drives outgassing chemistry and atmospheric composition of rocky planets. *Sci Rep* **10**, 10907.

Rielli A., Tomkins A. G., Nebel O., Brugger J., Etschmann B., Zhong R., Yaxley G. M. and Paterson D. (2017) Evidence of sub-arc mantle oxidation by sulphur and carbon. *Geochem. Persp. Let.*, 124–132.

Righter K. and Drake M. J. (1996) Core Formation in Earth's Moon, Mars, and Vesta. *Icarus* **124**, 513–529.

888 Righter K., Leeman W. P. and Hervig R. L. (2006a) Partitioning of Ni, Co and V between spinel-structured
889 oxides and silicate melts: Importance of spinel composition. *Chemical Geology* **227**, 1–25.

890 Righter K., Sutton S. R., Newville M., Le L., Schwandt C. S., Uchida H., Lavina B. and Downs R. T. (2006b)
891 An experimental study of the oxidation state of vanadium in spinel and basaltic melt with
892 implications for the origin of planetary basalt. *American Mineralogist* **91**, 1643–1656.

893 Rizo H., Walker R. J., Carlson R. W., Horan M. F., Mukhopadhyay S., Manthos V., Francis D. and Jackson
894 M. G. (2016) Preservation of Earth-forming events in the tungsten isotopic composition of modern
895 flood basalts. *Science* **352**, 809–812.

896 Roeder P. L. and Emslie R. F. (1970) Olivine-liquid equilibrium. *Contr. Mineral. and Petrol.* **29**, 275–289.

897 Saunders A. D., Fitton J. G., Kerr A. C., Norry M. J. and Kent R. W. (2013) The North Atlantic Igneous
898 Province. In *Geophysical Monograph Series* (eds. J. J. Mahoney and M. F. Coffin). American
899 Geophysical Union, Washington, D. C. pp. 45–93.

900 Shorttle O., Moussallam Y., Hartley M. E., Maclennan J., Edmonds M. and Murton B. J. (2015) Fe-XANES
901 analyses of Reykjanes Ridge basalts: Implications for oceanic crust's role in the solid Earth oxygen
902 cycle. *Earth and Planetary Science Letters* **427**, 272–285.

903 Starkey N. A., Stuart F. M., Ellam R. M., Fitton J. G., Basu S. and Larsen L. M. (2009) Helium isotopes in
904 early Iceland plume picrites: Constraints on the composition of high 3He/4He mantle. *Earth and*
905 *Planetary Science Letters* **277**, 91–100.

906 Stracke A., Hofmann A. W. and Hart S. R. (2005) FOZO, HIMU, and the rest of the mantle zoo.
907 *Geochemistry, Geophysics, Geosystems* **6**.

908 Suzuki T. and Akaogi M. (1995) Element partitioning between olivine and silicate melt under high
909 pressure. *Phys Chem Minerals* **22**.

910 Taracsák Z., Longpré M.-A., Tartèse R., Burgess R., Edmonds M. and Hartley M. E. (2022) Highly Oxidising
911 Conditions in Volatile-Rich El Hierro Magmas: Implications for Ocean Island Magmatism. *Journal of*
912 *Petrology* **63**, egac011.

913 Valbracht P. J., Staudigel H., Honda M., McDougall I. and Davies G. R. (1996) Isotopic tracing of volcanic
914 source regions from Hawaii: decoupling of gaseous from lithophile magma components. *Earth and*
915 *Planetary Science Letters* **144**, 185–198.

916 Wang J., Xiong X., Takahashi E., Zhang L., Li L. and Liu X. (2019) Oxidation State of Arc Mantle Revealed
917 by Partitioning of V, Sc, and Ti Between Mantle Minerals and Basaltic Melts. *Journal of Geophysical*
918 *Research: Solid Earth* **124**, 4617–4638.

919 Weaver B. L. (1991) The origin of ocean island basalt end-member compositions: trace element and
920 isotopic constraints. *Earth and Planetary Science Letters* **104**, 381–397.

921 Weiss Y., Class C., Goldstein S. L. and Hanyu T. (2016) Key new pieces of the HIMU puzzle from olivines
922 and diamond inclusions. *Nature* **537**, 666–670.

Willhite L. N., Jackson M. G., Blichert-Toft J., Bindeman I., Kurz M. D., Halldórsson S. A., Harðardóttir S., Gazel E., Price A. A. and Byerly B. L. (2019) Hot and Heterogenous High-3He/4He Components: New Constraints From Proto-Iceland Plume Lavas From Baffin Island. *Geochemistry, Geophysics, Geosystems* **20**, 5939–5967.

Workman R. K., Hart S. R., Jackson M., Regelous M., Farley K. A., Blusztajn J., Kurz M. and Staudigel H. (2004) Recycled metasomatized lithosphere as the origin of the Enriched Mantle II (EM2) end-member: Evidence from the Samoan Volcanic Chain. *Geochemistry, Geophysics, Geosystems* **5**.

Yaxley G. M. and Green D. H. (1994) Experimental demonstration of refractory carbonate-bearing eclogite and siliceous melt in the subduction regime. *Earth and Planetary Science Letters* **128**, 313–325.

Zhang X.-Y., Chen L.-H., Wang X.-J., Hanyu T., Hofmann A. W., Komiya T., Nakamura K., Kato Y., Zeng G., Gou W.-X. and Li W.-Q. (2022) Zinc isotopic evidence for recycled carbonate in the deep mantle. *Nat Commun* **13**, 6085.

Zindler A. and Hart S. (1986) Chemical Geodynamics. *Annual Review of Earth and Planetary Sciences* **14**, 493–571.